POLITECNICO DI TORINO

**Corso di Laurea Magistrale
in Ingegneria Matematica**

Tesi di Laurea Magistrale

Natural ventilation forced by wind fluctuations: theoretical analysis and experimental study

Relatori
prof. Luca Ridolfi
prof. Riccardo Vesipa
prof. Pietro Salizzoni

Candidata
Teresa Di Renzo

Marzo 2023

Summary

This study investigates the dynamics of a naturally ventilated room in which a point source provides a steady buoyancy source, when an opposing unsteady wind occurs. The wind is modelled as a stochastic forcing, which aims to simulate realistic velocity fluctuations as observed in the lower atmosphere, due to atmospheric turbulence. By doing so, we expand the analysis already conducted for deterministic wind, following both a theoretical approach and an experimental one. Firstly, regarding the theoretical approach, we compute some numerical simulations, which highlight how the stochastic forcing affects and changes the dynamics of the system. Namely, a structural change of the mean behaviour of the system occurs: the warm–cold air interface does not fluctuate around the elevation exhibited when wind is constant, but oscillations occur around a new interface elevation, which is significantly lower. We provide the physical explanation for such a counterintuitive behaviour and show its dependence on (i) wind characteristics (intensity and timescale of fluctuations) and (ii) relative strength of wind over thermal loads. Secondly, concerning the experimental approach, we perform some experiments in wind tunnel in order to compare the measures with the numerical results. The experimental results are in reasonable agreement with theoretical predictions, and confirm the key role of stochastic components in naturally ventilated systems.

Contents

List of Tables

List of Figures

9

Introduction

The natural ventilation of internal spaces is an approach enabling to take advantage of waste thermal loads (e.g. people, electrical devices) to bring fresh air inside an enclosed space (e.g. a room). The key process behind natural ventilation is the stack effect that arises from the presence of the buoyancy of warmer air over colder air [Linden et al., 1990, Linden, 1999, Hunt and Linden, 1999, Lishman and Woods, 2006, Yuan and Glicksman, 2007]. Thermal loads inside the room heat air, and the warm air tends to float over the surrounding colder air, reaching the ceiling of the room. On the ceiling, it accumulates and by doing so, it causes a pressure difference with respect with the external ambient. Such a phenomenon is the so-called stack effect. If the room presents an opening cut at the ceiling level (top opening) and another opening at floor level (bottom opening), the pressure difference forces the heated air out of the room through the top opening. This leak of fluid is replaced by air coming from the external ambient (thus, it concerns colder and fresh air) which enters through the bottom opening (see Figure 1.1).

The picture mentioned above illustrates as the natural ventilation of an enclosed space is based on the generation of a stack effect strong enough to expel warm air through the top opening and bring in some fresh air through the bottom opening. It follows that any phenomenon which can assist or contrast this effect has to be taken into account [Hunt and Linden, 2005, 2001, 1999]. In this context, wind plays a major role. As a matter of fact, by interacting with constructions, it generates pressure difference between the windward and leeward faces of the buildings [Montazeri and Blocken, 2013]. This way, depending on its strength and direction, wind can considerably change the dynamics of naturally ventilated systems. In particular, besides the strength, its effect depends on the position of the top opening [Hunt and Linden, 2005, 2001, 1999]: if the top opening is on the windward faces, wind contrasts the natural ventilation; if the top opening is on the windward face, wind assists the stack effect and thus the ventilation. In the first case - in case of the so-called "opposing" wind - if wind is strong enough, it can be overcomes the stack effect, inducing a fresh air inflow through the top opening.

Over the last decades, natural ventilation has received a great deal of attention from the scientific community. Such an interest stems from energy savings that can be obtained with this approach, reducing the energy demand of buildings. Furthermore, understanding the air flow path inside enclosed spaces allows us to quantify and predict the quality of indoor air [Yang et al., 2012, Bhagat et al., 2020]: by knowing how airborne diseases spread around, some issues related to air quality in enclosed spaces can be planned and solved. Despite the importance of this topic, the design of effective and robust ventilation system

11

based on the stack effect is still a challenging task. Indeed, the variability of the environmental parameters and the strong non-linearity of the dynamics of the system make the study of such phenomenon strongly complex. As a matter of fact, the interplay between fluctuating parameters and non-linear dynamics can trigger unexpected behaviours which can thwart the efficacy of natural ventilation. Thus, a key topic of research is understanding and considering the possible occurrence of these conditions, and proposing solutions for a more resilient ventilation. In this picture, this work aims to highlight the major and non-trivial effect of stochastic fluctuations of wind velocity on ventilation dynamics [Vesipa et al., 2023].

In previous works on this topic, a wide range of possible configurations of naturally ventilated enclosed spaces was covered; in particular, it were considered single [Woods et al., 2003, Kuesters and Woods, 2011] or multiple [Holford and Hunt, 2003, Hunt and Acred, 2013] rooms, with varying cross-sectional area with height [Economidou and Hunt, 2010], multiple [Kaye and Hunt, 2004] or distributed [Lishman and Woods, 2006, Yuan and Glicksman, 2007] sources of buoyancy. Most of the works assumed adiabatic walls, but cases of thermally conductive or thermally massive walls were also analysed [Lishman and Woods, 2009b, Lane-Serff and Sandbach, 2012].

Several peculiar behaviours of such ventilated systems can be explained by means of a simple modelling approach, which considering balances of volume and buoyancy gives rise to a system of coupled ordinary differential equations. Despite their simplicity - compared to much more complex fluid dynamics numerical approaches -, theoretical models show a remarkable agreement with observations and experiments performed in laboratory. This proves the riability of such modelling in simulating the dynamics of ventilation in both stationary [Heiselberg et al., 2004, Stavridou and Prinos, 2013, Hunt and Linden, 2005] and non-stationary [Coomaraswamy and Caulfiled, 2011, Mott and Woods, 2011] conditions.

Within this body of literature, one of the most interesting results concerns the effect of opposing wind, i.e. wind which contrasts the stack effect. Indeed, it can induce multiple steady states [Coomaraswamy and Caulfiled, 2011, Yuan and Glicksman, 2008, Hunt and Linden, 2005]. Namely, under the same forcing conditions - i.e. same wind velocity and same thermal loads - the system can exhibit either a "stratified forward flow" regime or a "mixed reverse flow" regime. In the first case, buoyancy forces are stronger than wind inertial forces and the ejection of air through the top opening is maintained; in the second case, wind forces overcome buoyancy forces and an inflow of air from the top opening occurs, resulting in ejection of air through the bottom opening. As it typically happens for a bistable dynamical system, the ventilation regime which occurs depends on its previous history.

In order to describe systems that actually take place in real word, it is necessary to consider the effect of its unsteadiness which come from environmental conditions (e.g., unsteady wind velocity) or from internal uses (e.g., varying thermal loads). Recent works focused on these effects; in particular wind gusts (described as fluxes of cold air entering in a warm room [Mott and Woods, 2011, 2012]), periodic changes of thermal load [Bower et al., 2008, Bolster, 2008], sudden changes in wind velocity [Lishman and Woods, 2009a, Craske and Hughes, 2019], transient scenarios (e.g., a cold room where thermal loads are suddenly turned on [Coomaraswamy and Caulfiled, 2011]) were investigated.

In the studies conducted so far, unsteadiness processes were simulated by means of deterministic models. This approach revealed successful in showing peculiar features of the dynamics of unsteady naturally ventilated systems (e.g., hysteresis phenomena, bistability occurrence, stability of the equilibrium points to finite-amplitude perturbations), but it can only partially describe phenomenon. As a matter of fact, this deterministic approach is unsuitable to consider typical environmental unsteadiness exhibited by wind. Wind dynamics is characterised by a strong variability over a wide range of temporal scales. Noticeably, it is intrinsically stochastic, as it exhibits random fluctuations both in intensity [Edwards and Hurst, 2001] and direction [Doorn et al., 2000]. Such fluctuations arise due to turbulent nature of atmospheric flows [Arenas-López and Badaoui, 2020] and due to interaction of wind with bluff bodies (e.g., trees and buildings) placed upstream the ventilated system considered [Mora-Pérez et al., 2015].

In recent years, it has been shown that random fluctuations can have a relevant and counterintuitive effect on the behaviour of dynamical systems, especially in case of nonlinear processes [Ridolfi et al., 2011, Vesipa et al., 2015, 2016, 2021]. For this reason, since ventilates systems are characterised by nonlinear processes, we expect that occurrence of stochastic wind fluctuations can considerably change the dynamics of the system. So far, this aspect was considered only by Fontanini et al. [2013], who showed as stochastic wind forcing and stochastic fluctuatiuons of thermal loads can significantly alter the response of the system, compared to its behaviour in case of deterministic wind velocity and thermal load. Such a difference results in a reduction of the efficacy of natural ventilation.

However, Fontanini et al. [2013] focused only on the case of distributed buoyancy sources. Such condition avoids the generation of a warm buoyant layer in the room. Moreover, they did not study the role of the parameters that characterise the stochastic forcing (e.g., magnitude and time scale of the fluctuations) and the ventilated system (e.g., mean wind velocity, mean thermal load, room size and geometry, opening size).This way, there are still several aspects concerning the stochastic forcing of naturally ventilated systems that have not been investigated yet. One of the most relevant aspect regards the role of wind stochasticity on ventilated systems where a warm buoyant layer arises and an opposing wind occurs. Since these systems are bistable, their dynamics are likely to be highly affected by the presence of random fluctuations in the wind forcing [Vesipa et al., 2023, Ridolfi et al., 2011].

As done by a previous work by Vesipa et al. [2023], we expand the analysis performed by Coomaraswamy and Caulfiled [2011] focusing on the effect of wind randomness on the dynamics of the warm-cold layer stratification in a naturally ventilated room. Whereas the study by Vesipa et al. [2023] focused just on a theoretical approach, this work aims to validate the theoretical results obtained by performing an experimental campaign and comparing the measures with the theoretical outcomes. In order to do that, firstly we present the physical phenomenon and the mathematical model, giving the system of equations which govern the natural ventilation of a room in presence of a point buoyancy source and an opposing wind (Chapter 1). Then, in Chapter 2, we introduce the model of random fluctuations considered, namely an additive stochastic forcing in the governing equations. We report the solutions of such equations, numerically solved by an explicit Runge-Kutta approach. The results highlight how the stochastic forcing affects the dynamics of the room: the time-average dynamical equilibrium configuration attained

in case of stochastic forcing can be much different from the equilibrium conditions reached in case of constant wind. We show the dependence of such difference on (i) wind characteristics (intensity and timescale of fluctuations) and (ii) relative strength of wind over thermal loads. Later, in Chapter 3, we give an explanation of the phenomenon and an analytical solution for the average values around which the dynamics of the system fluctuates. We compare such a solution with numerical simulations. Finally, in Chapter 4, the experimental campaigned is described and the results reported. The measures are in agreement with the outcomes of the theoretical study: the alteration of the time-averaged dynamics of the ventilated system is observed and the key role of stochastic component of wind dynamics is confirmed.

Chapter 1

Mathematical Model and Numerical Method

In order to investigate the natural ventilation of a room, we consider a representative system - commonly adopted in the relevant literature [Coomaraswamy and Caulfiled, 2011, Hunt and Linden, 2005] - which is naturally ventilated. Specifically, we study the behaviour of a transient flow in a room containing two openings and a single localised heat source, by using a simplified model. This model consists in a cubic box of height H which contains an isolated buoyancy point source at floor level, one ceiling-level opening and one floor-level opening. The opening areas are assumed to be smaller than the cross-sectional area of the room; under this assumption the pressure is expected to vary approximately hydrostatically in the interior.

From the buoyancy source a plume of warm fluid rises, due to thermal convection. Since the thermal plume has a different density compared to the ambient air density, warm fluid and ambient air do not mix, but remain separated. For this reason, when the thermal plume reaches the ceiling it accumulates, forming a buoyant layer which do not contain cooler and more dense ambient air. This way, a two-layer stratification arises from the opposition between the flow driven by the plume and the ambient air. As a result, we observe an upper layer of warm fluid that lies above a lower layer of cool ambient fluid. The interface between the warm air and the fresh air is located at height h above the floor. In this situation, the warm air generates a pressure difference between the two layers that produces a stack effect driving the room ventilation. In Figure 1.1 a schematic diagram for displacement ventilation is presented. Note that we assume that the Boussinesq approximation holds: in such an approximation the density difference between the warm layer and the exterior environment is considered small, compared to a reference density, i.e. the ambient density.

Note that in our discussion we assume the density of the upper layer to be uniform at all times, as a result of the turbulence of the plume. This means that we are making an assumption of instantaneous and perfect mixing throughout this upper layer. Such an assumption is valid when the time scale for mixing is much shorter than the time scale

for movement of the interface between the two layers. From this assumption it follows that the reduced gravity of the upper layer is independent of the vertical coordinate z and denoted by g'.

In steady state conditions, due to volume conservation, the net flow rate through all openings is zero. Then, the amount of warm fluid expelled from the top opening is equal to the amount of ambient air blown in through the bottom opening; these flow rates are equal to the volume flux in the plume at height h.
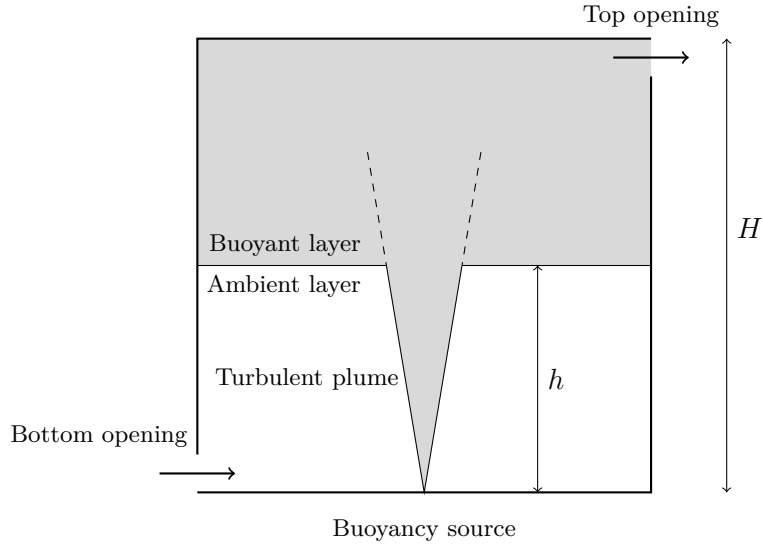
Figure 1.1: Schematic diagram for displacement ventilation considered in this study. A room with a single localised heat point source is considered. The point source generates a plume of warm fluid and a stratification takes place: an upper layer of warm fluid sits above a lower layer of cool ambient fluid. In this case ventilation occurs through the bottom opening (cool air inlet) and the top opening (warm air outlet).

The presence of wind, and the strength of wind, can radically change this situation. In Figure 1.1, where the stratification takes places, effects of wind are not taken into account, and the stack effect is not overwhelmed. However, if the wind is strong enough, the ventilation of the room can experience major changes. Nevertheless, note that we do not take into account wind strong enough to violate the hydrostatic conditions in the interior.

In order to investigate the wind effects, we discern between wind which either assist or contrast the natural ventilation of the room. Their effects are different indeed. In particular, in case of assisting wind, the cool ambient air is drawn in through the bottom opening while the warm air is expelled from the top opening. Therefore the interface between the warm layer and the cool layer h moves towards a higher level. This situation is shown in Figure 1.2.

In case of opposing wind more scenarios can occur, depending on the strength of the
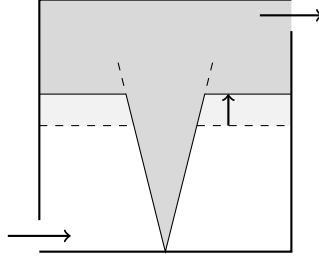
Figure 1.2: Schematic diagram for displacement ventilation in case of assisting wind. The fresh ambient air is drawn in through the low-level opening, while the warm fluid is expelled from the high-level opening. The interface between the two layers moves towards a higher level, i.e. $\hat{h}$ increases.

wind. Indeed the stack effect is preserved if the wind is weak enough; otherwise, if the wind is strong enough, it overcomes the stack effect and a reverse flow occurs. Therefore, besides the forward flow regime, also reverse flow regimes can take place. Hence in case of opposing wind three different regimes can be observed. All these regimes are represented in Figure 1.3. Let us show in detail the differences between these regimes.

(a) Regime $\mathcal{A}$ (b) Regime $\mathcal{B}$ (c) Regime $\mathcal{C}$
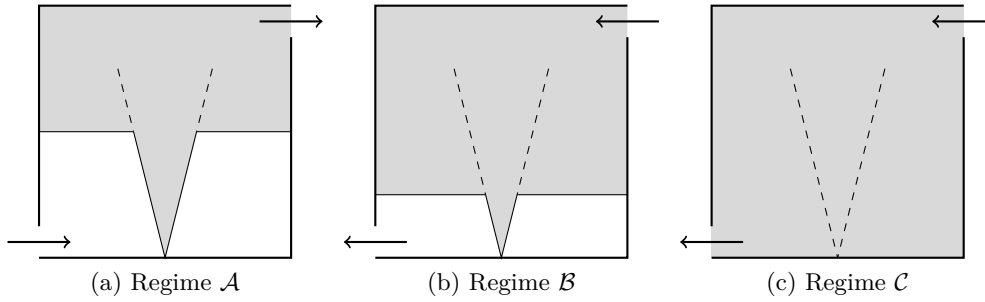
Figure 1.3: Schematic diagrams of the possible regimes in case of opposing wind. 1.3a: buoyancy-driven flow regime, which is a forward flow regime with two-layer stratification. 1.3b: wind-driven flow regime, that is a reverse flow with two-layer stratification. It is purely transient, i.e. no steady state can exist in this regime. 1.3c: wind-driven flow regime, which is a reverse flow with a well-mixed layer that occurs since the box is fully contaminated.

- In the forward flow regime (schematized in Figure 1.3a), which is buoyancy-driven, the wind is weak enough to preserve the stack effect. Then cool ambient air is still blown into the bottom opening, and warm fluid still leaks out from the top opening, but the wind reduces the outflow, and then it also decreases the inflow. We will refer to this regime as regime $\mathcal{A}$.

- In the first reverse flow (Figure 1.3b), the wind is strong enough to overcome the stack effect. In this wind-driven regime fresh ambient air is drawn in through the high-level opening and it cools the warm fluid in the upper layer. At the floor level, air is expelled from the low-level opening and no cool fluid enters. In this case the

two-layer stratification is maintained, but the interface h moves gradually towards lower levels. We will make reference to this regime as regime $\mathcal{B}$.

- After some time, if regime $\mathcal{B}$ persists, the second reverse flow regime occurs (Figure 1.3c); in this case the interior of the box is fully contaminated with plume fluid, so that $h = 0$. As a result, we observe a single well-mixed layer. Also in this case, ambient air is drawn in through the top opening, and the mixed air leaks out from the bottom opening. We will refer to this regime as regime $\mathcal{C}$.

Note that regime $\mathcal{B}$ is purely transient: if it persists for some time, necessarily regime $\mathcal{C}$ occurs. Otherwise, if the wind strength reduces, the system goes back to regime $\mathcal{A}$. It is therefore clear that no steady state can exist in regime $\mathcal{B}$.

As we will see in the following, for constant wind strength, a two-layer steady state governed by regime $\mathcal{A}$ can be reached for all wind strengths. On the other hand, for sufficiently strong wind, two wind-driven steady states described by regime $\mathcal{C}$ (one stable and one unstable) can also exist. Besides the strengths of the buoyant source and the wind, realisation of one stable state rather than the other one depends on initial conditions, rate of variation in wind strength and the timescale over which the wind is increased.

1.1   Mathematical model

1.1.1   Description of the problem and its parameters

Let us describe in detail our model and its parameters, keeping in mind the schematic diagram in Figure 1.1.

We consider a box of height H and uniform cross-sectional area A_C. The buoyancy point source, placed at the floor level, releases a pure buoyancy flux of strength B_0. We define the effective area A^* of the openings as

$$A^* = \frac{\sqrt{2}c_B A_B c_T A_T}{\sqrt{c_B^2 A_B^2 + c_T^2 A_T^2}},$$ (1.1)

where A_T, c_T and A_B, c_B are the area and the discharge coefficient of the top opening and the bottom opening, respectively. The discharge coefficient takes into account the dissipative losses of flow through the associated opening, dependent on its geometry and the pattern of the flow through it.

Regarding the plume, it has been observed that plumes are geometrically self-similar [Batchelor et al., 2003, Morton et al., 1956, Baines and Turner, 1969]. In particular, the rising fluid is observed to take a mean conical shape. It means that the velocity and temperature distributions across the plume have the same profiles at any height above the source. Depending on the height, the amplitudes and the widths of the distributions vary. This way, all the properties of the plume depend only on the vertical height z and on the

buoyancy flux strength B_0. Such an observation allows us to simplify the problem and the equations which govern the problem, since the vertical height and the buoyancy strength are sufficient to determine all the properties of the plume. However, we will consider another assumption: the entrainment assumption. The reason it has been introduced in the literature is that in some circumstances, such as when a stratified environment occurs, scaling arguments cannot be applied. This assumption comes from the hypothesis that the inflow velocity at the plume edge, i.e. the entrainment velocity u_e defined by

$$bu_e = -ru\big|_{\text{plume edge}},$$

where b is the mean radius of the cone defined at any height, r is the radial coordinate, u is the horizontal component of the velocity field, is proportional to the mean vertical velocity w in the plume at any height. Thus, the entrainment assumption reads as

$$u_e = \alpha w, \tag{1.2}$$

where α is the entrainment constant. The entrainment assumption leads to the same plume volume fluxes obtained from similarity theory for an unstratified fluid. Since the entrainment assumption is more general than the assumption deriving from similarity theory, it has been preferred.

Coming back to our problem, we are interested in the behaviour and the temporal variation of two variables: the steady state-state interface height h between the two layers, and reduced gravity g' in the upper layer.

It is useful to consider the dimensionless variable $\hat{h} = h/H$ instead of h; reminding the 'top-hat' entrainment constant α for a plume introduced above and introducing a non-dimensional parameter V describing the vent area, once we have defined

$$C = \left(\frac{6\alpha}{5}\right)\left(\frac{9\alpha\pi^2}{10}\right)^{1/3},$$

the non-dimensional interface height $\hat{h}$ satisfies

$$V = \left(\frac{A^*}{C^{3/2}H^2}\right)^2 = \frac{\hat{h}^5}{(1 - \hat{h})}. \tag{1.3}$$

From classical plume theory [Morton et al., 1956] and 'filling-box' studies [Baines and Turner, 1969, Worster and Huppert, 1983], it was showed that steady-state interface $\hat{h}$ is independent of the source buoyancy flux B. Note that the same argument can be deduced by observing that between the three independent quantities controlling the flow, namely A^*, B, H, the source buoyancy flux B is the only quantity containing the dimensions of time, and hence, the steady-state position of the interface is independent of B [Hunt and Linden, 2001].

In order to define the reduced gravity, which is the change in the acceleration of gravity acting on a fluid in contact with another fluid of different density due to buoyancy forces, let us denote the density of the ambient fluid ρ and the density of the upper layer $\rho - \Delta\rho$; thus, the reduced gravity in the upper layer reads $g' = g\Delta\rho/\rho$. We notice that the reduced

gravity in the upper layer is equal to its value within the plume at height h above the floor, since it does not depend on the vertical coordinate z; then

$$g' = g'_P = C^{-1} B_0^{2/3} h^{-5/3}. \tag{1.4}$$

We are assuming that each layer is well-mixed and that the only exchange of fluid between the two layers occurs just through the plume. Therefore, in case of absence of wind, the volume flux Q_T through the top opening balances the volume flux Q_P through the plume at height h:

$$Q_T = A^* [g'(H - h)]^{1/2} = Q_P = C B_0^{1/3} h^{5/3}. \tag{1.5}$$

Note that the sign of Q_T depends on the direction of the flow: if $Q_T > 0$ warm buoyant air is expelled through the top opening; if $Q_T < 0$ cool ambient air is blown in through it.

Due to the opposing fluid flows, a difference Δp_b in the ambient pressure between the top opening and the bottom opening arises. Recalling that we are considering hydrostatic conditions inside the box, we assume that Stevin's law holds; thus $p(z) - p_0 = -\rho g z$. We can set $p_0 = 0$. In absence of buoyancy layer, the pressure at any height z reads $p(z) = -\rho g z$ (where ρ is the density of ambient air, as already mentioned). In case of presence of buoyancy layer, we have to discern between the lower layer and the upper layer. Indeed, the pressur is given by

$$p(z) = \begin{cases} -\rho g z & \text{if } z \leq h, \\ -\rho g h - \rho_u g (z - h) & \text{if } z > h, \end{cases}$$

where ρ_u is the density of air in the warmer layer. As a consequence, at height $z = H$ the pressure difference induced by the buoyancy is equal to $\Delta p_b = (\rho_u - \rho) g (H - h) = \rho g'(H - h) < 0$; the subscript b stands for "bouyancy". Due to this pressure difference a stack effect arises, which drives the room ventilation. Furthermore, in case of presence of wind, the picture can change since wind induces a further forcing on the system. It happens due an additional difference pressure between the building facades, which reads

$$\Delta p_w = \frac{1}{2} \rho \left(C_{pu} - C_{pl} \right) v^2, \tag{1.6}$$

where v is the wind velocity, and C_{pu}, C_{pl} are the wind pressure coefficients for the upper and the lower openings, respectively. The subscript w stands for "wind". We can denote by $C_p = C_{pu} - C_{pl}$ the total wind pressure coefficient for the room. Note that $\Delta p_w < 0$, i.e. $C_{pu} < C_{pl}$, means that the low-opening is on the windward side while the high-level opening is on the leeward side; in this case, the wind assists the ventilation inside the room. On the other hand, when $\Delta p_w > 0$, i.e. $C_{pl} < C_{pu}$, the low-opening is on the leeward facade and the high-opening is on the windward side; thus, for $\Delta p_w > 0$ the wind contrasts the ventilation. In the following we will denote by Δp the total difference pressure, which takes into account the pressure difference induced by the buoyancy and, in case of presence of wind, the forcing induced by the wind. Note that in case of $\Delta p_w > 0$, the pressure difference induced by the buoyancy and the pressure difference induced by the wind have opposite sign.

We can now define the non-dimensional wind strength W dependent on the difference of pressure:

$$W = \frac{\Delta p_w / \rho}{g'_H H}. \tag{1.7}$$

Here g'_H is the reduced gravity in the plume when it reaches the top of the box, i.e.

$$g'_H = g'_P\big|_{h=H} = C^{-1} B_0^{2/3} H^{-5/3}. \tag{1.8}$$

By performing a dimensional analysis, we observe that both the numerator and the denominator of Equation 1.8 are dimensionally equivalent to the square of a velocity. Indeed

$$\left[\frac{\Delta p_w}{\rho}\right] = \frac{\text{kg}}{\text{ms}^2} \cdot \frac{\text{m}^3}{\text{kg}} = \left(\frac{\text{m}}{\text{s}}\right)^2,$$

$$[g'_H H] = \frac{\text{m}}{\text{s}^2} \cdot \text{m} = \left(\frac{\text{m}}{\text{s}}\right)^2.$$

For this reason, the square root of the wind strength $\sqrt{W}$ can be considered as a Froude number, namely the ratio between the velocity associated with the wind pressure drop ($\sqrt{\Delta p_w / \rho}$), and the velocity associated with the buoyancy in the enclosure ($\sqrt{C^{-1}(B_0/H)^{2/3}}$):

$$Fr = \sqrt{W}. \tag{1.9}$$

1.1.2 Governing equations

Regarding the upper layer where the density of the warm fluid is assumed to be uniform at all times, conservation of mass yields

$$A_C \frac{d}{dt}[(H-h)] = Q_P - Q_T. \tag{1.10}$$

On the other hand, conservation of buoyancy yields

$$A_C \frac{d}{dt}[g'(H-h)] = \begin{cases} Q_P g'_P - Q_T g', & \text{if } Q_T > 0 \\ Q_P g'_P. & \text{if } Q_T < 0 \end{cases} \tag{1.11}$$

Then using 1.10 we can rewrite 1.11 as

$$A_C(H-h)\frac{dg'}{dt} = \begin{cases} Q_P(g'_P - g'), & \text{if } Q_T > 0 \\ Q_P(g'_P - g') + Q_T g', & \text{if } Q_T < 0 \end{cases} \tag{1.12}$$

which is an equivalent expression for conservation of buoyancy.

Note that we are considering two different separate cases for $Q_T > 0$ and $Q_T < 0$; as already seen, $Q_T > 0$ corresponds to forward flow, while $Q_T < 0$ corresponds to reverse flow.

We observe that regarding the plume, expressions for Q_P and g'_P are given by 1.5 and 1.4, respectively. On the other hand, for the top opening we have to supply a different

expression for the volume flux, which takes into account the presence of wind. Hence we have

$$Q_T = \begin{cases} A^* \left[g'(H-h) - \frac{\Delta p_w}{\rho} \right]^{1/2}, & \text{if } Q_T > 0 \\ -A^* \left[\frac{\Delta p_w}{\rho} - g'(H-h) \right]^{1/2}. & \text{if } Q_T < 0 \end{cases} \qquad (1.13)$$

We notice that a strictly positive difference $\Delta p_w > 0$ in ambient pressure between the two openings corresponds to opposing wind; a difference in ambient pressure arises from the presence of wind indeed. If the difference in pressure is null, $\Delta p_w = 0$, no opposing wind occurs and the volume flux through the top opening is equal to the volume flux through the plume.

What we have seen so far holds if the interior of the box is not fully contaminated with plume fluid. In fully contaminated regime, the interface reaches the floor and the evolution equation is different due to the fact that the interface remains at the bottom of the box:

$$h = \frac{dh}{dt} = 0. \qquad (1.14)$$

Then, conservation of buoyancy reads

$$A_C H \frac{dg'}{dt} = Q_P g'_P - Q_B g', \qquad (1.15)$$

where Q_B is the volume flux out of the bottom opening and it is given by

$$Q_B = A^* \left[\frac{\Delta p}{\rho} - g'H \right]. \qquad (1.16)$$

Equations seen in this section (1.10-1.15) together form a set of governing equations which model flow in each of the regimes we have taken into account.

1.1.3 Non-dimensionalisation

We are interested in finding a non-dimensional form for the governing equations of our problem. In order to obtain such a set of equations, we define the dimensionless variables

$$\hat{h} = h/H \qquad \text{and} \qquad \hat{g} = g'/g'_H, \qquad (1.17)$$

which are the variables whose evolution in time we want to study. In such an equation, g'_H is given by 1.8.

To non-dimensionilising time, three different and independent time scales are suitable; then we have to find a criterion to choose one of them. Each time scale can be constructed by dividing the volume of the box $A_C H$ by a different scaling for flow rate: it is the particular scaling for flow rate which determines the time scale. Then we refer as T_{Bf} to the buoyancy-driven 'filling box' time scale, as T_{Bd} to the buoyancy-driven 'draining box' time scale, and as T_W to the wind-driven time scale. These time scales read, respectively,

$$T_{Bf} = \frac{A_c H}{C B_0^{1/3} H^{5/3}} = \frac{A_C}{C B_0^{1/3} H^{2/3}}, \tag{1.18a}$$

$$T_{Bd} = \frac{A_c H}{A^* (g'_H H)^{1/2}} = \frac{A_C C^{1/2} H^{4/3}}{A^* B_0^{1/3}}, \tag{1.18b}$$

$$T_W = \frac{A_C H}{A^* (\Delta p_w / \rho)^{1/2}}. \tag{1.18c}$$

In order to choose the time scale, we notice that T_{Bd} and T_W depend on the effective area A^* and the difference in ambient pressure Δp; since it is our intention to vary these two parameters to study their effect on our problem, we wish to avoid a non-dimensionalisation in time with respect to a time scale which depends on them. Hence we are led to opt for the buoyancy-driven 'filling box' time scale T_{Bf}. It depends on the buoyancy flux strength B_0, which we will keep fix in our study. Therefore let us define the non-dimensional time $\hat{t} = t/T_{Bf}$.

Now we notice that the dimentionless parameters V and W, whose definitions are given by 1.3 and 1.7 respectively, are equal to the square of a ratio of time scales:

$$V = \left(\frac{A^*}{C^{3/2} H^2} \right)^2 = \left(\frac{T_{Bf}}{T_{Bd}} \right)^2, \tag{1.19}$$

$$W = \frac{\Delta p_w / \rho}{g'_H H} = \left(\frac{T_{Bd}}{T_W} \right)^2. \tag{1.20}$$

1.1.4 Dimentionless governing equations

Now our aim is write down the governing equations 1.10-1.15 in a non-dimensional form for our dimensionless variables $\hat{h}$ and $\hat{g}$ defined in 1.17. In order to do that, we use the buoyancy-driven 'filling box' time scale T_{Bf} given by 1.18a; it means that we compute the temporal derivative in 1.10-1.15 with respect to the dimensionless time variable $\hat{t} = t/T_{Bf}$ instead of t.

By way of example, to show how the dimensionless governing equation have been obtained, we rewrite the mass conservation equation 1.10 computing the time derivative with respect to $\hat{t}$, when $Q_T > 0$. To do that, let us recall definitions 1.5, 1.13 of the plume and top fluxes, equation 1.3 regarding the effective area, definitions 1.4 and 1.7 of the reduced gravity and the wind strength. Thus we rewrite

$$
\begin{aligned}
A_C \frac{d}{dt}[(H - h)] &= Q_P - Q_T = C B_0^{1/3} h^{5/3} - A^* \left[g'(H - h) - \frac{\Delta p_w}{\rho} \right]^{1/2} \\
&= C B_0^{1/3} h^{5/3} - A^* (H g'_H)^{1/2} [\hat{g}(1 - \hat{h}) - W]^{1/2} \\
&= C B_0^{1/3} h^{5/3} - C B_0^{1/3} H^{5/3} V^{1/2} [\hat{g}(1 - \hat{h}) - W]^{1/2}.
\end{aligned}
\tag{1.21}
$$

Now observing that

$$A_C \frac{d}{dt}[(H - h)] = A_C H \frac{d}{d\hat{t}}[1 - \hat{h}] \frac{C B_0^{1/3} H^{5/3}}{A_C H},$$

and dividing 1.21 by $CB_0^{1/3}H^{5/3}$, we obtain

$$-\frac{d\hat{h}}{d\hat{t}} = \hat{h}^{5/3} - V^{1/2}[\hat{g}(1-\hat{h}) - W]^{1/2}.$$

Computing calculation for all the equations that form the set of governing equations 1.10-1.15, we find our dimensionless governing equations:

$$-\frac{d\hat{h}}{d\hat{t}} = \begin{cases} \hat{h}^{5/3} - |VP|^{1/2} & (\mathcal{A}) \\ \hat{h}^{5/3} + |VP|^{1/2} & (\mathcal{B}) \\ 0 & (\mathcal{C}), \end{cases} \qquad (1.22a)$$

$$\frac{d}{d\hat{t}}[\hat{g}(1-\hat{h})] = \begin{cases} 1 - |VP|^{1/2}\hat{g} & (\mathcal{A}) \\ 1 & (\mathcal{B}) \\ 1 - |VP|^{1/2}\hat{g} & (\mathcal{C}). \end{cases} \qquad (1.22b)$$

By writing the letters, we are referring to the regimes explained in the introduction of this chapter, and shown in Figure 1.3. As already mentioned in 1.1.2, we have to consider separate cases for $Q_T > 0$ and $Q_T < 0$, indeed. We notice that $Q_T > 0$ corresponds to forward flow, which is governed by regime $\mathcal{A}$; on the other hand, in case of reverse flow, $Q_T < 0$ holds and either regime $\mathcal{B}$ or regime $\mathcal{C}$ occur. Then we can allude to these different cases by referring to the relevant regime instead of the sign of Q_T.

Furthermore we notice that by using this scaling we highlight the quantity P, which appears in 1.22. It is given by

$$P = \hat{B} - W. \qquad (1.23)$$

Since W is the wind strength while $\hat{B} = \hat{g}(1 - \hat{h})$ represents the dimensionless buoyancy in the warm layer, P can be interpreted as the resulting balance between the competing effects of wind and buoyancy. Then, P can be seen as a measure of the dimensionless pressure at the top of the opening. Note that the direction of the flow thus is also determined by the sign of P: for $P > 0$ buoyancy forces are stronger than wind strength, resulting in a buoyancy-driven forward flow (regime $\mathcal{A}$, $Q_T > 0$); for $P < 0$ wind strength is predominant on buoyancy forces, then wind-driven reverse flow occurs (regime $\mathcal{B}$ and $\mathcal{C}$, $Q_T < 0$).

Summarising, the three regimes explained at the beginning of the chapter and shown in Figure 1.3 can be characterized by considering the sign of P (or Q_T) and the value of $\hat{h}$. Note that by looking just at the sign of P (or Q_T) we cannot distinguish between regime $\mathcal{B}$ and $\mathcal{C}$. Therefore we characterize the different regimes taking into account also the value of $\hat{h}$, in the following way.

- Regime $\mathcal{A}$, with buoyancy-driven forward flow and a two-layers stratification, occurs when $P \geq 0$ and $\hat{h} \geq 0$.

- Regime $\mathcal{B}$, with wind-driven reverse flow, keeps a two-layers stratification; it means that it occurs when $P < 0$ and $\hat{h} > 0$.

- Regime $\mathcal{C}$, with wind-driven reverse flow and the interior of the box fully contaminated with plume fluid, occurs when $P < 0$ and $\hat{h} = 0$.

1.1.5 Equilibrium states

Let us now focus on equilibrium states reached by the system when V and W keep constant values in time. Equilibrium states are characterized by a dimensionless interface height $\hat{h}_{eq}$ and a dimensionless reduced gravity $\hat{g}_{eq}$ which do not vary in time but remain constant. It follows that in equilibrium states the effects of the buoyancy force, and its competition with wind, do not change; thus also $\hat{g}_{eq}(1 - \hat{h}_{eq})$ keeps a constant value.

In order to find steady solutions for the system 1.22, we have to set the temporal derivative of $\hat{h}$ and $\hat{g}(1 - \hat{h})$ equal to 0.

Concerning regime $\mathcal{A}$, we find

$$\begin{cases} \hat{h}^{5/3} = \sqrt{\left| V \left[\hat{g}(1 - \hat{h}) - W \right] \right|} \\ 1 = \sqrt{\left| V \left[\hat{g}(1 - \hat{h}) - W \right] \right|} \hat{g}, \end{cases}$$

thus

$$\hat{g}_{eq} = \hat{h}_{eq}^{-5/3}, \qquad V = \frac{\hat{h}_{eq}^{10/3}}{\hat{h}_{eq}^{-5/3}(1 - \hat{h}_{eq}) - W}. \tag{1.24}$$

This is the buoyancy-driven steady state. It exists for any value of V and W.

Regarding regime $\mathcal{C}$, for which $\hat{h}_{eq}$ is equal to 0, we find

$$V(\hat{g}_{eq} - W) = 1,$$

and then

$$\hat{g}_{eq}^3 - W \hat{g}_{eq}^2 + V^{-1} = 0. \tag{1.25}$$

Solutions in regime $\mathcal{C}$ are given by the roots of 1.25. A pair of real positive roots exists if and only if

$$W^3 V > 27/4. \tag{1.26}$$

Thus wind-driven steady states do not exist for any values of V and W; if $W^3 V < 27/4$ no wind-driven steady state exist, while if $W^3 V > 27/4$ two solutions occur, one stable and one unstable.

Note that we do not consider steady states in regime $\mathcal{B}$ because it is purely transient.

For what has been explained, it is clear that $W^3 V = 27/4$ is a bifurcation point: when $W^3 V < 27/4$ only regime $\mathcal{A}$ is possible, regardless of the initial conditions. Conversely, for wind strength strong enough to have $W^3 V > 27/4$, two stable configurations are possible: one configuration is regime $\mathcal{A}$, while the other one is regime $\mathcal{C}$. Therefore, if $W^3 V > 27/4$ the initial conditions determine which regime will govern the system. The

attractor basins of the two stable configurations are separated by the unstable solution, which is the second solution related to regime $\mathcal{C}$. In Figure 1.4 the steady states $\hat{h}_{eq}$ (1.4a) and $\hat{g}_{eq}$ (1.4b) are shown as function of the wind strength W. Black lines correspond to stable solutions: the solid ones are stable states governed by regime $\mathcal{A}$, the dashed ones are the stable steady states governed by regime $\mathcal{C}$. The grey dashed lines correspond to unstable solutions driven by regime $\mathcal{C}$. Note that the two solutions of $\hat{h}$ for regime $\mathcal{C}$ coincide, since in both cases $\hat{h} = 0$; then the two lines overlap (see Figure 1.4a). The vertical dotted line corresponds to the bifurcation point $W^3V = 27/4$: solutions governed by regime $\mathcal{C}$ exist only to the right of this line.

(a) Steady state solutions for $\hat{h}$　　　(b) Steady state solutions for $\hat{g}$
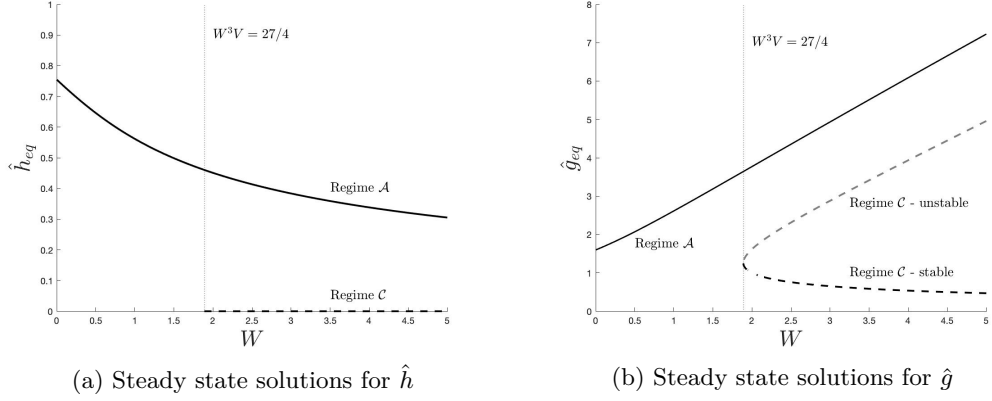
Figure 1.4: Steady states solutions of the systems 1.22 for $\hat{h}$ (1.4a) and $\hat{g}$ (1.4b). Vertical dotted line corresponds to the bifurcation point $W^3V = 27/4$; both the charts refer to $V = 1$. The continuous black line corresponds to solution for regime $\mathcal{A}$; it exists for any value of W. The dashed line refers to the two solutions for regime $\mathcal{C}$; they exist only for $W^3V > 27/4$. One of them is stable (black line), while the other one is unstable (grey line). Note that in 1.4a the two solutions for regime $\mathcal{C}$ overlap and they both are equal to $\hat{h}_{eq} = 0$. No steady state solution exists for regime $\mathcal{B}$.

1.2　Numerical method and theoretical results for steady opposing wind

Given a set of initial conditions, the coupled pair of nonlinear ODEs 1.22 for the dimensioless variables $\hat{h}$ and $\hat{g}$ can be integrated numerically for any values of V and W. In particular, we used the MATLAB function `ode45`, which is an ODE solver based on an explicit Runge-Kutta formula and which is a single-step solver.

In the following we will show the time series evaluated with the developed numerical method for constant V and W. Later we will show the phase diagrams of $\hat{g} - \hat{h}$ space, to better understand the behaviour of the system.

1.2.1 Time series with steady opposing wind

Once we have developed the numerical method, we now validate it applying it to the simplest problem we can consider: the filling of a box initially fully filled with fresh ambient fluid, in the presence of a constant opposing wind. It means that we consider constant wind strength W, besides constant V. By considering a box which is initially fully filled with ambient air, we are setting the initial condition:

$$\hat{t} = 0 : \quad \hat{h} = 1, \quad \hat{g} = 1. \tag{1.27}$$

We have computed the time evolution of $\hat{h}$ and $\hat{g}$ for four different finite value of wind strength keeping $V = 1$ fixed, namely $W = 0,1,1.5,2$. In Figure 1.5 the time series of $\hat{h}$ and $\hat{g}$ are shown. Blue solid lines correspond to $W = 0$, red solid lines to $W = 1$, yellow solid lines to $W = 1.5$, purple solid lines to $W = 2$.

(a) Time series of $\hat{h}$ (b) Time series of $\hat{g}$
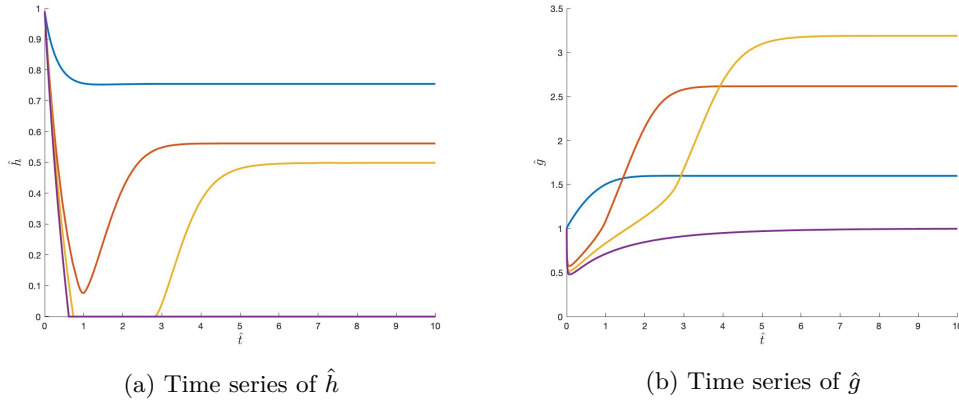
Figure 1.5: Time series of $\hat{h}$ (1.5a) and $\hat{g}$ (1.5b) when opposing wind has constant strength and $V = 1$. In particular, blue solid lines corresponds to $W = 0$; red solid lines to $W = 1$; yellow solid lines to $W = 1.5$; purple solid lines to $W = 2$.

The case $W = 0$ corresponds to absence of wind. The value of $\hat{h}$ slightly decreases while the value of $\hat{g}$ slightly increases; both settle on the stable values after a short time.

In case of presence of wind, we observe a different behaviour. Regarding $\hat{h}$ there is a non null difference between the final equilibrium interface height $\hat{h}_{eq}$ and the minimum interface height reached in the time series $\hat{h}_{min}$. Such an overshoot increases dramatically as the wind strength W increases: looking at the red solid line in Figure 1.5a we notice that for $W = 1$ the overshoot is almost half of the box height, much greater than the maximum possible in case of absence of wind ($W = 0$). Keeping looking at the red solid line in 1.5a and taking into account also the red line in 1.5b, we observe that for early times the system is governed by regime $\mathcal{B}$. Indeed, $P = \hat{g}(1 - \hat{h}) < 0$ and $\hat{h} > 0$ (recall subsection 1.1.4). In this case (when $W = 1$) a fully contaminated scenario does not occur, and regime $\mathcal{C}$ does not take place. Therefore, a buoyancy-driven steady state is reached. In general, the time in which the flow changes direction slightly precedes the

27

time when the interface height reaches its minimum value. In this particular case, these times almost coincide, at $\hat{t} = 1$.

For larger wind strength, the interface approaches the floor and regime $\mathcal{C}$ occurs. For $W = 1.5$ (solid yellow line in Figure 1.5), a fully contaminated scenario takes place. Nevertheless after some time the system once more switches regime: a new interface starts to rise from the floor, reaching a buoyancy-driven steady state value. It is different the case of $W = 2$; for such a stronger wind strength, once the interface has reached the floor, its height keeps the value $\hat{h} = 0$. The system remains fully contaminated and it reaches a wind-driven steady state.

As it is clear by looking at Figure 1.5b, when $W > 0$, $\dfrac{d\hat{g}}{d\hat{t}}$ is singular at $\hat{h} = 1$. It is due to the fact that an infinitely thin upper layer can change temperature infinitely quickly, in order to change into a temperature which balances the cooling due to fresh ambient air and the heating due to the thermal plume. For this reason, in our numerical simulations we have set as initial condition $\hat{h} = 0.99$ instead of $\hat{h} = 1$ for $\hat{t} = 0$.

1.2.2 Phase diagram for constant V and W

In order to study stability and basins of attraction, it is useful to consider phase diagram of $\hat{g}$ and $\hat{h}$.

It is possible to conduct such a study because when V and W keep constant values, the nonlinear dynamical system 1.22 is autonomous; therefore evolution equations concerning $\hat{g}$ and $\hat{h}$ have no explicit dependence on $\hat{t}$ and thus it is possible to generate phase diagrams.

In Figure 1.6 four phase diagrams are presented, for cases $V = 1$, $W = 0,1,1.5,2$. In each phase diagram, for each point in the $\hat{h} - \hat{g}$ space, a vector is plotted: it represents the magnitude and sign of $\dfrac{d\hat{g}}{d\hat{t}}$ and $\dfrac{d\hat{h}}{d\hat{t}}$. All these vectors are normalized, resulting in arrows of equal length. The thin dotted black line correspond to the curve given by $\hat{g} = \hat{h}^{-5/3}$. Note that our model applies only for $\hat{g} < \hat{h}^{-5/3}$; therefore, in the region above and to the right of this curve our model is not valid and we ignore this area. The reason is that above and to the right of this curve, the fluid in the upper layer is less cold and less dense than the the fluid that is injected by the plume. In this situation, the assumption that the upper is well-mixed is doubtful; therefore our model is not applicable for $\hat{g} > \hat{h}^{-5/3}$. On the other hand, along $\hat{g} = \hat{h}^{-5/3}$ the temperature of fluid in the warm layer is equal to the temperature of fluid injected by the plume; indeed, it is a condition of equilibrium, as we have already found in subsection 1.1.5. Recalling 1.24, it is clear that for any W, buoyancy-driven equilibria must lie on this curve.

The thick black lines, which are drawn when $W > 0$, correspond to $P = 0$. Hence, to the right of these curves, $P > 0$ and the regions are of forward flow; on the other side, to the left of the curves, $P < 0$ and the regions are of reverse flow. The red lines are trajectories corresponding to the initial conditions $\hat{h} = \hat{g} = 1$. In figure 1.6d green lines are trajectories corresponding to four different initial conditions; in particular, these initial conditions are the equilibrium states reached for $W = 0,0.5,1,1.5$ starting form $\hat{h} = \hat{g} = 1$.

By observing Figure 1.6a, we can study the behaviour of the system in absence of wind

(a) $W = 0$

(b) $W = 1$

(c) $W = 1.5$

(d) $W = 2$
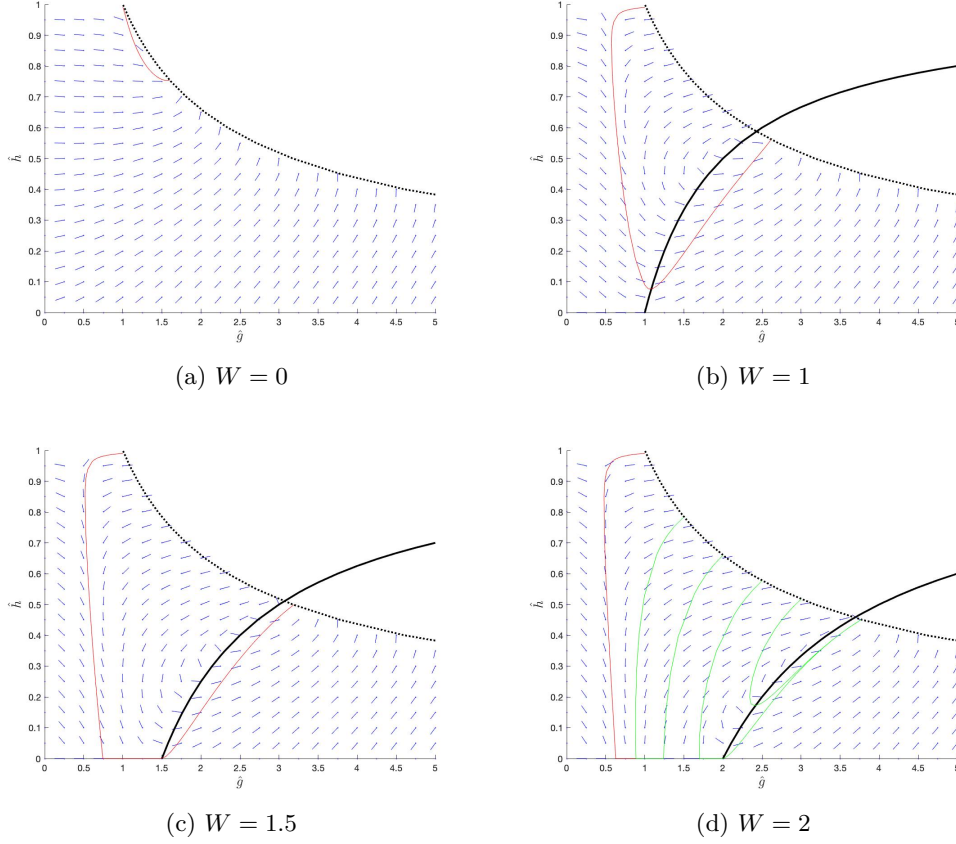
Figure 1.6: Phase diagrams for $V = 1$ and $W = 0$ (1.6a), $W = 1$ (1.6b), $W = 1.5$ (1.6c), $W = 2$ (1.6d). Thin black dotted lines correspond to $\hat{g} = \hat{h}^{-5/3}$; recall that our model applies only for the region under this curve. Thick black lines correspond to $P = 0$; thus it separates the region of forward flow (on the right of the curve) and the region of reverse flow (on the left). Note that in 1.6a only region of forward flow appears. At each point in the $\hat{g} - \hat{h}$ space a vector is plotted, indicating the magnitude and the sign of $d\hat{g}/d\hat{t}$ and $d\hat{h}/d\hat{t}$ in that point. Red lines are trajectories starting from $\hat{h} = \hat{g} = 1$. In 1.6d, green lines are trajectories for four different initial conditions, which are the equilibrium states reached for $W = 0, 0.5, 1, 1.5$ starting form $\hat{h} = \hat{g} = 1$.

($W = 0$). We notice that the buoyancy-driven steady state is a global attractor: each trajectory, whose direction can be observed by looking at the direction of the vectors, reaches the curve $\hat{g} = \hat{h}^{-5/3}$. Hence, each trajectory approaches an equilibrium state that is proper to bouyancy-driven steady state. This steady state is a stable focus. In this case, since $W = 0$, the curve corresponding to $P = 0$ is not displayed and the whole space is of forward flow.

In case of $W > 0$, a region of reverse flow appears to the left of the curve $P = 0$. Nevertheless, for $W = 1$ and $W = 1.5$, the buoyancy-driven steady state is still a global attractor, as we can notice observing Figures 1.6b, 1.6c. Indeed, by looking at the trajectories starting starting from $\hat{h} = \hat{g} = 1$ and more in general at the vectors

represented, we observe that reverse flow and a fully contaminated transient can occur before the system reaches the steady states, which still lie on the curve $\hat{g} = \hat{h}^{-5/3}$ and are buoyancy-driven. Then, wind-driven steady states do not occur yet.

For larger wind strength, also wind-driven steady states appear, as we can appreciate by looking at Figure 1.6d. In this case, where $W = 2$, the trajectory starting from $\hat{h} = \hat{g} = 1$ approaches $\hat{h} = 0$ and remains on this value. However, wind-driven steady state is not a global attractor. As we can notice by looking at the green trajectories, there exist some initial conditions such that a reverse flow and a fully contaminated transient occur before the system reaches a buoyancy-driven steady state. It means that it is still possible to approach the buoyancy-driven state, even if a wind-driven state exists. Hence, two basins of attraction exist: one for each stable steady state. The basin of attraction of the buoyancy-steady state lies along the curve $\hat{g} = \hat{h}^{-5/3}$, while the basin of the wind-driven steady state lies along $\hat{h} = 0$. It has been observed that keeping fixed V and increasing W, the stable buoyancy-driven steady state moves down and to the right, always along the curve $\hat{g} = \hat{h}^{-5/3}$; on the other side, the basin of attraction of the wind-driven steady state moves to the left along $\hat{h} = 0$ and increases.

It is interesting to observe that the system has a hysteric response to increments or decrements in wind strength. To appreciate this behaviour, let us consider Figure 1.6d and let us recall that the green trajectories start from the steady states reached for $W = 0,0.5,1,1.5$ when the starting condition is $\hat{h} = \hat{g} = 1$. We can notice that a jump in wind strength from $W = 0$ or $W = 0.5$ to $W = 2$ would mean a jump from buoyancy-driven steady state to wind-driven equilibrium state; on the other hand, a jump in wind strength from $W = 1$ or $W = 1.5$ would maintain the steady state of the system buoyancy-driven. Indeed, starting from the initial condition $\hat{h} = \hat{g} = 1$ with $W = 1$ or $W = 1.5$ leads to a steady state on the $\hat{g} = \hat{h}^{-5/3}$ curve; approached the steady state, if the wind strength increases up to $W = 2$ reverse flow occurs, but the system still reach a buoyancy-driven equilibrium state. Therefore, small increments in wind strength does not cause a transition to wind-driven steady state; on the contrary, it is possible to remain in the buoyancy-driven state indefinitely. However, increasing W the basin of attraction of this state moves down and to the right of the $\hat{g} = \hat{h}^{-5/3}$ curve, becoming very small and unstable, until wind-driven state occurs. Conversely, small decrements in wind strength allow the system to remain in a wind-driven state until the critical point $W^3 V = 27/4$ is reached. Below such a point the wind-driven steady state cannot exist.

Chapter 2

Stochastic wind fluctuations

So far we have investigated equilibrium states and we have simulated the behaviour of $\hat{h}$ and $\hat{g}$ in case of steady opposite wind. By doing so, we have followed a deterministic approach. However, in real cases, wind exhibits a strong variability. Indeed wind dynamics is intrinsically stochastic, as it exhibits random fluctuations in strength and direction. It follows that a deterministic approach can only partially describe the phenomenon.

For this reason we want to expand the analysis that has been conducted for deterministic wind, taking into account wind randomness as done by Vesipa et al. [2023]. Our aim is to understand how the presence of a stochastic wind, instead of a deterministic wind, affects the dynamics of natural ventilated systems.

2.1 Generation of time series of $W(t)$

2.1.1 Wind velocity fluctuations

In turbolent flow fluid dynamics it is common to express the stochastic variables as a sum of a mean value and fluctuations around it. We apply this approach to the wind dynamics, by writing the wind velocity as

$$v(t) = \bar{v} + v'(t), \tag{2.1}$$

where $\bar{v}$ is the mean velocity and $v'(t)$ is the time-dependent fluctuation around $\bar{v}$. In order to model such a fluctuation we adopt the Ornstein-Uhlenbeck stochastic process [Uhlenbeck and Ornstein, 1930, Gu et al., 2020], which is widely used in wind engineering. Such a process is a stationary colored Gaussian-Markov process with the following particular characteristics:

- the probability density function of the realizations $v'(t)$ is a Gaussian distribution with zero mean and standard deviation σ_{wv}, where the subscript wv stands for "wind velocity";

- the stochastic process is exponentially autocorrelated as

$$\langle v'(t)v'(t+\tau)\rangle = \sigma_{wv}\exp[-\tau/\tau_{wv}],$$

where $\langle\cdot\rangle$ denotes the ensemble average operator and τ_{wv} is the autocorrelation time (or relaxation time);

- the process is stationary, i.e. σ_{wv} and τ_{wv} do not change over time.

Beside these characteristics, the Ornstein-Uhlenbeck process has several analytical properties. Among all, we have chosen the Ornstein-Uhlenbeck process as the random velocity fluctuation due to its simplicity, mathematical tractability, and the possibility of changing its variance and (linear) memory by acting on only two parameters, namely the standard deviation σ_{wv} and the autocorrelation timescale τ_{wv}.

Once introduced the stochastic process, fluctuation dynamics can be modelled as [Gillespie, 1996]

$$\mathrm{d}v'(t) = av'(t)\,\mathrm{d}t + b\,\mathrm{d}\Omega(t), \tag{2.2}$$

where $\Omega(t)$ is the standard Brownian motion while a and b are two constants, namely $a = -\tau_{wv}^{-1}$ and $b = c_{wv}^{1/2}$, where $c_{wv} = 2\sigma_{wv}^2/\tau_{wv}$ is the so-called "diffusion constant". It follows that we can rewrite the standard deviation σ_{wv} as

$$\sigma_{wv} = \sqrt{-\frac{1}{a} \cdot \frac{b^2}{2}} = \sqrt{\tau_{wv}\frac{c_{wv}}{2}}. \tag{2.3}$$

In Tab 2.1 values of a and b provided by Ma et al. [2018] are reported, with the corresponding relaxation time τ_{wv} and standard deviation σ_{wv}.

a	b	$\tau_{wv}(s)$	$\sigma_{wv}(m/s)$	$v_{0,min}(m/s)$	$v_{0,max}(m/s)$
-0.1619	0.2878	6	0.51	4.00	8.00
-0.0855	0.1700	12	0.41	8.00	9.40
-0.0314	0.2573	32	1.03	9.40	10.20
-0.1049	0.3137	10	0.68	10.20	10.70
-0.0459	0.5118	22	1.69	10.70	11.20
-0.0196	0.2901	51	1.47	11.20	12.00
-0.0683	0.4051	15	1.10	12.00	12.80
-0.0957	0.3008	10	0.69	12.80	25

Table 2.1: Parameters a and b provided by Ma et al. [2018] with their corresponding relaxation times τ_{wv} and standard deviation σ_{wv}. Their relative values $v_{0,min}$ and $v_{0,max}$ delimit the range of values of mean wind velocity within which the parameters are valid.

2.1.2 Generation of time series in a dimentional framework

In order to generate time series of the wind parameter $W(t)$, three steps are required:

1. generation of stochastic time series $v(t)$;

2. generation of time series of the wind parameter $W(t)$;

3. generation of time series of the wind parameter depending on non-dimentional time $W(\hat{t})$.

Let us see in details what these steps consist in, recalling that we are considering a dimensional framework for now.

In order to generate the stochastic time series $v(t)$ we use the so-called "Exact numerical update formula of the Ornstein-Uhlenbeck process" [Gillespie, 1996]. By using it, for fixed values of σ_{wv} and τ_{wv}, we can obtain a realization of the velocity fluctuations time series $v'(t)$, namely

$$v'(t + \Delta t) = v'(t) \cdot \zeta + \sigma_{wv} \cdot \sqrt{1 - \zeta^2} \cdot n, \tag{2.4}$$

where n is a random number from a zero-mean unit-variance Gaussian distribution, Δt is the time-step of the process, and $\zeta = \exp\left[-\Delta t / \tau_{wv}\right]$.

The importance of being able to obtain realizations of the velocity fluctuations lies in the fact that we use them to generate the time series of the wind parameter $W(t)$, which is the second step. In order to do that, let us recall Equations 1.4 and 1.6 and let us substitute them in Equation 1.7. By doing so we immediately obtain

$$W(t) = \frac{CH^{2/3}\left(C_{pu} - C_{pl}\right)}{2B_0^{2/3}} v^2(t). \tag{2.5}$$

By defining

$$\chi = \frac{CH^{2/3}\left(C_{pu} - C_{pl}\right)}{2B_0^{2/3}}, \tag{2.6}$$

we can rewrite Equation 2.5 as

$$W(t) = \chi v^2(t). \tag{2.7}$$

In the end, the final step requires to introduce a dimentionless time scale. In order to define it, let us recall from Equation 1.18a the buoyancy-driven 'filling box' time scale T_{Bf}, chosen to non-dimensionalize the equations. Then, we can define the non-dimentional time $\hat{t} = t/T_{Bf}$ so that

$$W(\hat{t}) = W\left(\frac{t}{T_{Bf}}\right) = \chi v^2\left(\frac{t}{T_{Bf}}\right) = \chi v^2(\hat{t}). \tag{2.8}$$

Note that temporal scaling also requires to take into account the time step Δt and the relaxation time τ_{wv}. The dimentionless time step $\Delta \hat{t}$ and relaxation time $\hat{\tau}_{wv}$ are obtained by directly dividing Δt and τ_{wv} by the buoyancy-driven 'filling box' time scale T_{Bf}.

2.1.3   Generation of time series in a dimentionless framework

Once we have obtained the time series of $W(\hat{t})$ in a dimentional framework, we need to generate the time series in a dimentionless framework. In order to do that, let us recall Equation 2.8. We can notice that when the velocity is constant and there are not fluctuations, i.e. $v(\hat{t}) = v_0$, also the wind parameter $W(\hat{t})$ is constant; indeed, $W(\hat{t}) = \chi v_0^2 = W_0$. It follows that $\chi = W_0/v_0^2$, and then we can rewrite Equation 2.8 in case of variable wind velocity as

$$W(\hat{t}) = \chi v^2(\hat{t}) = \frac{W_0}{v_0^2} v^2(\hat{t}) = W_0 \left[\frac{v_0 + v'(\hat{t})}{v_0} \right]^2 . \tag{2.9}$$

By writing the time series of $W(\hat{t})$ in this way, we highlight the two key ingredients. The first ingredient is the mean value of the wind parameter W_0. The second ingredient is given by the factor

$$\left[\frac{v_0 + v'(\hat{t})}{v_0} \right]^2 .$$

It is a great result because it means that all the dimentional parameters which compare in the definition of the wind parameter W (Equation 1.7) are not required to evaluate W from v. Instead, it is sufficient to provide a mean value of the wind parameter, W_0.

Furthermore, we have to make a remark concerning the term $v_0 + v'(\hat{t})/v_0$. This term shows that the magnitude of wind velocity fluctuations alone is not a key factor: fluctuations magnitude has to be referred to the mean value of the velocity v_0, indeed. For this reason, it is more convenient to consider the coefficient of variation of the wind velocity $C_{V,wv} = \sigma_{wv}/v_0$ rather than the standard deviation of the wind velocity σ_{wv}. By doing so, we focus on the coefficient of variation of the wind speed, without evaluating the velocity in dimensional terms. It results in a key advantage.

2.2   Results

We investigate the effect of stochastic wind velocity fluctuations on the behaviour of the ventilation dynamics of a room - i.e., on the interface height $\hat{h}(\hat{t})$ and the reduced gravity $\hat{g}(\hat{t})$ - by performing some numerical simulations [Vesipa et al., 2023]. Any of them consists in two steps.

Firstly, we set the room parameter (the vent parameter V) and the wind characteristics (i.e. the mean wind W_0 and the fluctuations properties, $\hat{\tau}_{wv}$ and $C_{V,wv}$). In order to choose the values for these parameters, typical literature values and real world data were used. Then, according to 2.4, the time series of the wind velocity fluctuations was simulated, and thus the corresponding time series of the wind parameter $W(\hat{t})$ was computed using 2.9. Note that the same series of random numbers n was maintained in order to keep the results comparable (thus the simulations differ for the values of $V, W_0, \hat{\tau}_{wv}, C_{V,wv}$).

Secondly, Equations 1.22 were forced with $W(\hat{t})$ and numerically solved in order to obtain the time series of the layer interface elevation $\hat{h}(\hat{t})$ and of the reduced gravity $\hat{g}(\hat{t})$. To compute that, the initial conditions $\hat{h}(\hat{t} = 0) = \hat{h}_0$ and $\hat{g}(\hat{t} = 0) = \hat{g}_0$ were set. Specifically,

the values $\hat{h}_0$ and $\hat{g}_0$ correspond to the equilibrium configurations obtained from Eq. 1.24 (regime $\mathcal{A}$) or Eq. 1.25 (regime $\mathcal{C}$) setting $W = W_0$. To compute the numerical integration, an explicit Runge-Kutta approach was used. Built-in MATLAB routines and functions (`ode45`) were used. The time duration of the simulations was set equal to $4000\tau_{wv}$, so that $\hat{h}(\hat{t})$ and $\hat{g}(\hat{t})$ could reach the statistical steady state.

2.2.1 Zero-mean wind fluctuations alter the average elevation of the warm-cool air interface

In order to investigate the effects of the stochastic forcing on the system dynamics, we consider few emblematic examples. To highlight the main peculiarities of the stochastic forcing case compared to the constant wind case, it is useful to define and consider two metrics:

- $\eta(\hat{t}) = \frac{\hat{h}(\hat{t})}{\hat{h}_0}$,

- $\gamma(\hat{t}) = \frac{\hat{g}(\hat{t})}{\hat{g}_0}$,

where $\hat{h}_0$ and $\hat{g}_0$ refer to the equilibrium states reached in Regime $\mathcal{A}$ and evaluated by Eq. 1.24, or in Regime $\mathcal{C}$ and evaluated by Eq. 1.25. So that, $\eta(\hat{t})$ and $\gamma(\hat{t})$ describe the behaviour of $\hat{h}(\hat{t})$ and $\hat{g}(\hat{t})$ compared to the constant wind case. Furthermore, $\eta(\hat{t})$ and $\gamma(\hat{t})$ quantify the deviation of the system dynamics when the system is forced by a stochastically varying wind from the dynamics of the same system when the wind is constant and a stratified forward flow takes place (Regime $\mathcal{A}$). Thus, the values $\eta = \gamma = 1$ indicate that no modifications occur from the constant wind case; whereas $\eta < 1$ and $\gamma < 1$ indicate that both the layer interface elevation and the reduced gravity are lower than those in the constant wind case. The values $\eta > 1$ and $\gamma > 1$ would stand for higher interface height and reduced gravity than those in the case not stochastically forced; as we will see in the following, this case never occurs.

In Figure 2.1 the time series of η and γ evaluated for $V = 1, C_{V,wv} = 0.1, \tau_{wv} = 0.005$ and $W = 1, 1.5, 2$ are reported.

Firstly, we consider as initial conditions $\hat{h}(\hat{t} = 0) = \hat{h}_0$ and $\hat{g}(\hat{t} = 0) = \hat{g}_0$ the ones evaluated by using Eq. 1.24; thus at $\hat{t} = 0$ the system is in an equilibrium configuration driven by a stratified forward flow, namely Regime $\mathcal{A}$. The corresponding time series $\eta(\hat{t})$ and $\gamma(\hat{t})$ are plotted in Figure 2.1 by using thick continuous lines: the black one corresponds to $W_0 = 1$, the blue one to $W_0 = 1.5$ and the red one to $W_0 = 2$. For all the three considered cases we observe a similar temporal pattern:

(i) at $\hat{t} = 0$ the system is at equilibrium conditions found at the steady state, i.e. $\eta(\hat{t} = 0) = \gamma(\hat{t} = 0) = 1$;

(ii) over the time interval $0 < \hat{t} \lesssim 2$, η and γ reduce significatevely;

(iii) for $\hat{t} \gtrsim 2$ the system stabilises on a new condition of dynamic equilibrium around which $\eta(\hat{t})$ and $\gamma(\hat{t})$ oscillate, due to the persistent random forcing.
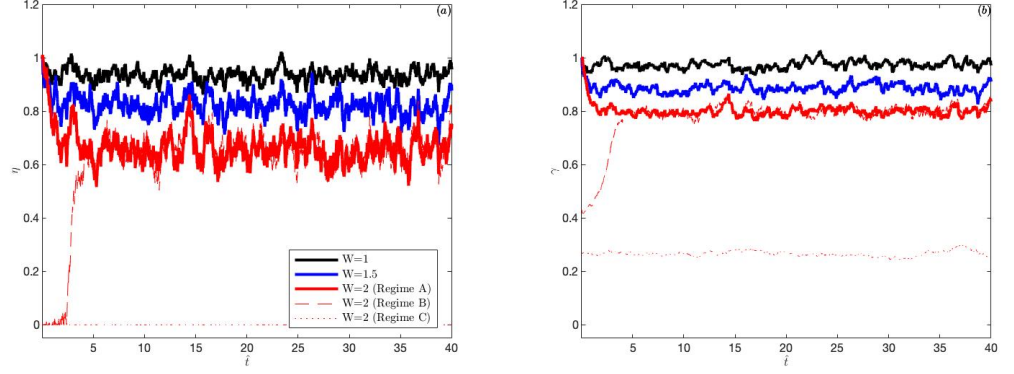
Figure 2.1: Time series of η (a) and γ (b) for different values of W_0, namely $W = 1, 1.5, 2$. The other parameters are set as $V = 1, C_{V,wv} = 0.1$ and $\tau_{wv} = 0.005$. Thick continuous lines refer to initial conditions evaluated by Eq. 1.24, corresponding to the equilibrium configuration driven by Regime $\mathcal{A}$. Black lines correspond to $W_0 = 1$, blue lines to $W_0 = 1$ and red lines to $W_0 = 2$. Dotted red line and dashed red lines refer to initial condition evaluated by Eq. 1.25 and corresponding to the stable and unstable configuration of Regime $\mathcal{C}$, respectively.

Note that the larger W_0 is, the larger the deviations of η and γ from unity are, and the larger the amplitude of fluctuations of η are (during the dynamic equilibrium phase). We observe that on the other hand, fluctuations of γ are less sensitive to the magnitude of W_0.

Secondly, we focus on the initial conditions $\hat{h}(\hat{t} = 0) = \hat{h}_0$ and $\hat{g}(\hat{t}) = \hat{g}_0$ evaluated from Eq. 1.25. Indeed, since $W_0 = 2$ is beyond the bifurcation threshold $W_0^3 V > 27/4$, for this case we can consider as initial conditions the equilibrium configuration driven by mixed backward flow in case of constant wind. It means that at $\hat{t} = 0$ the system is governed by Regime $\mathcal{C}$. Note that the two initial conditions have the same value for $\hat{h}_0 = 0$, but two different values for $\hat{g}_0$: indeed one refers to the stable equilibrium, the other one to the unstable one. In Figure 2.1, the dashed red line refers to the case in which the initial condition is the unstable one, whereas the dotted red line refers to the simulation having as initial condition the stable one. We notice that the case corresponding to the unstable equilibrium configuration exhibits a transient phase which leads the system to the same condition of dynamic equilibrium reached by the system when the initial condition is evaluated by Eq. 1.24. On the other hand, when the initial condition is the stable equilibrium state, the system is almost insensitive to wind fluctuations: $\eta(\hat{t})$ remains constant at the value $\eta(\hat{t}) = 0$, while $\gamma(\hat{t})$ exhibits small fluctuations.

We can observe a further feature of the emblematic examples previously discussed. A stochastic perturbation with zero mean added to a constant wind induces the system to oscillate with zero-mean fluctuations around a dynamic equilibrium, but the mean value of this dynamic equilibrium is not equal to the steady configuration of equilibrium reached in case of constant wind. As a matter of facts, the stochastic noise alters the averaged behaviour of the system (compared to the system forced by a constant wind), and it induces a reduction in the layer interface elevation and the reduced gravity.

2.2.2 Effects of noise parameters

It is interesting to analyse the role of the wind forcing - i.e. $W_0, C_{V,wv}$ and $\hat{\tau}_{wv}$ - and the geometric characteristics of the building, i.e. V. In order to do that, it is useful to define the average interface height η_{eq} and the average reduced gravity γ_{eq} attained during the dynamical equilibrium phase as

$$\eta_{eq} = \frac{1}{T_{fin} - T_{eq}} \int_{T_{eq}}^{T_{fin}} \eta(t)\,\mathrm{d}t, \tag{2.10}$$

$$\gamma_{eq} = \frac{1}{T_{fin} - T_{eq}} \int_{T_{eq}}^{T_{fin}} \gamma(t)\,\mathrm{d}t, \tag{2.11}$$

where T_{eq} and T_{fin} delimit the temporal range of the dynamical equilibrium phase.

In Figure 2.2 the influence of the coefficient of variation of the wind velocity $C_{V,wv}$ and of the correlation time $\hat{\tau}_{wv}$ on η_{eq} and γ_{eq} is shown. The venting parameter is fixed as $V = 1$, while W_0 assumes values equal to 1,1.5,2. In the figure, the values of $C_{V,wv}$ are reported on the x-axis; whereas the dimentionless correlation time varies from 0.05, which corresponds to the highest curve for each value of W_0, to 0.15, which corresponds to the lowest curve. The values of $\hat{\tau}_{wv}$ in between these two boundaries are represented by the shaded areas. Some key features can be observed.
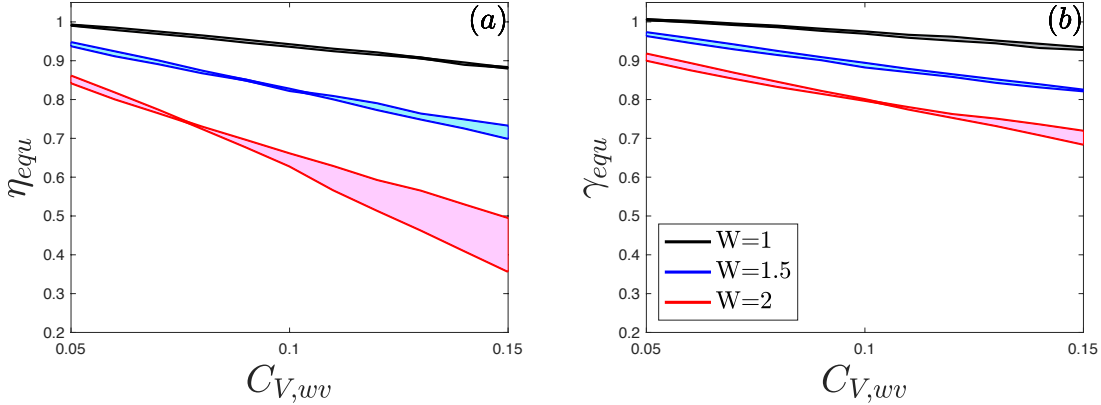
Figure 2.2: Effect of the noise parameter $C_{V,wv}$ on the averaged interface elevation η_{eq} (a) and reduced gravity γ_{eq} (b). The venting parameter is set $V = 1$, while the mean value of the wind parameter takes values $W_0 = 1,1.5,2$. The dimentionless correlation time $\hat{\tau}_{wv}$ varies from 0.05, which corresponds to the highest curve for each value of W_0, to 0.15, which corresponds to the lowest curve. The values of $\hat{\tau}_{wv}$ in between these two boundaries are represented by the shaded areas.

Firstly, dynamic equilibrium configurations obtained with a fluctuating wind parameter $W(t)$ can be very different from the equilibrium configurations in case of constant $W(t) = W_0$. These differences are relevant in a wide portion of the parameter space $\{C_{V,wv}, \hat{\tau}_{wv}\}$. In particular, for the parameter space considered we notice that the minimum value that η_{eq} attains is 0.65, while the minimun value of γ_{eq} is 0.35. It means that

wind fluctuations can reduce by 1/3 the layer interface elevation and by 2/3 the reduced gravity, compared to the constant wind case.

Secondly, the influence of the coefficient of variation of wind velocity $C_{V,wv}$ is very high both on η_{eq} and γ_{eq}. Indeed, for small values of $C_{V,wv}$, both η_{eq} and γ_{eq} are close to unity; on the other hand, as $C_{V,wv}$ increases, they reduce significantly.

Thirdly, the correlation time of wind velocity $\hat{\tau}_{wv}$ plays a minor role. It is more impacting on η_{eq} than on γ_{eq}, and it is more relevant for higher values of $C_{V,wv}$.

It is interesting to briefly discuss the different impact that $C_{V,wv}$ and $\hat{\tau}_{wv}$ have on η_{eq} and γ_{eq}. High values of $C_{V,wv}$ correspond to high deviation of $W(t)$ from W_0; whereas high values of $\hat{\tau}_{wv}$ correspond to long temporal duration of the deviation of $W(t)$ from W_0. As already observed, $C_{V,wv}$ is more impacting than $\hat{\tau}_{wv}$. This suggests that the magnitude of the deviation of $W(t)$ from W_0 is more relevant on the deviation of η_{eq} and γ_{eq} from unity than the duration of the time interval in which $W(t)$ deviates from W_0.

Fourthly, the mean value of the wind parameter W_0 has a significant role. Systems characterized by low magnitude of mean wind are barely affected by its fluctuations; by contrast, systems whose mean wind is elevated are more affected by the stochastic perturbation. We can notice this behaviour by observing that in Figure 2.2 the black curves barely deviate from unity, whereas the red curves exhibit larger deviations from unity.

2.2.3 Influence of ventilation parameter and mean wind intensity

We investigate now the influence of the ventilation parameter V and the wind parameter W_0 on the average interface elevation η_{eq} and the average reduced gravity γ_{eq}. We simulated all the combinations of $C_{V,wv} \times \hat{\tau}_{wv}$ in the range $[0.05, 0.10, 0.15] \times [0.01, 0.05, 0.10]$ for each pair $\{V, W_0\}$; among all the values of η_{eq} and γ_{eq} obtained, we report the minimum values attained, which occurred always for $C_{V,wv} = 0.15$ and $\hat{\tau}_{wv} = 0.10$. The results are shown in Figure 2.3: Fig. 2.3a, 2.3c show the influence of V and W_0 on η_{eq}, while Fig. 2.3b, 2.3d on γ_{eq}.

We can observe three different zones. The first zone, which is denoted in yellow, is characterized by values $\eta_{eq} \sim 1$ and $\gamma_{eq} \sim 1$, and it corresponds to low values of V and/or W_0. Low values of V correspond to a buoyancy-dominated dynamics, due to either a strong buoyancy source or very small openings; on the other hand, low values of W_0 mean a weak wind. In both cases, the effect of the wind is barely significant, and thus the effect of its fluctuations.

The second zone, the one denoted in blue, witnesses values $\eta_{eq} \sim 0$ and $\gamma_{eq} \sim 0$, and correspond to high values of both V and W_0. It highlights the influence of wind on the system dynamic. In this area of the space parameters, the mixed reverse flow (i.e. Regime $\mathcal{C}$) usually occurs. As already noticed in Figure 2.1 in section 2.2.1, in this case the wind
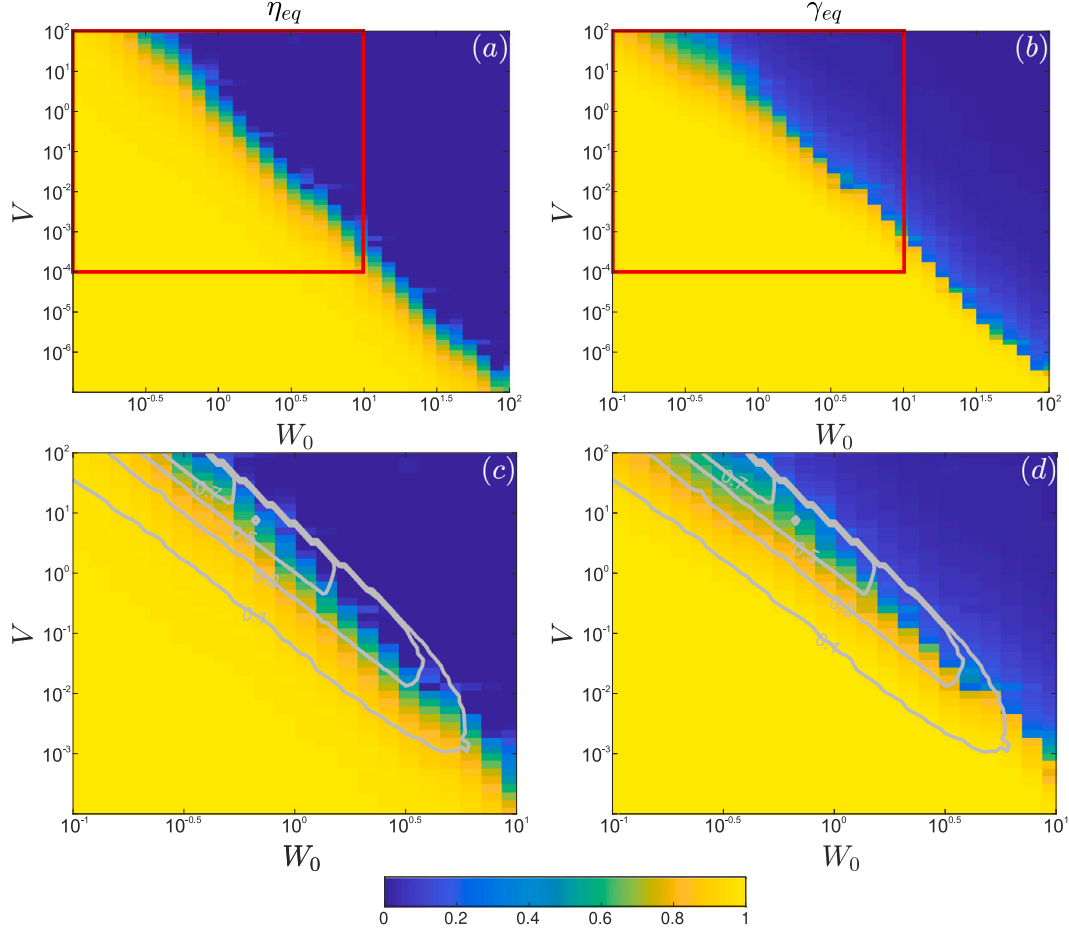
Figure 2.3: Effect of venting parameter V and mean of wind parameter W_0 on η_{eq} (a) and γ_{eq} (b). The figure reports the largest attained deviation of both η_{eq} and γ_{eq} from unity. The coefficient of variation of wind velocity $C_{V,wv}$ and the relaxation time $\hat{\tau}_{wv}$ span the range $[0.05,0.10,0.15] \times [0.01,0.05,0.10]$; the minimum values attained of η_{eq} and γ_{eq} (reported in the figure) occur always for $C_{V,wv} = 0.15$ and $\hat{\tau}_{wv} = 0.10$. Red rectangles delimit the zoomed view shown in panels (c) and (d). The gray curves in panels (c) and (d) are iso-lines of the "overshoots" $\hat{h}0 - \hat{h}_{min}$, as defined by Coomaraswamy and Caulfiled [2011].

fluctuations are not very relevant, and the buoyancy layer does not exist.

In the third zone, in which the colours change from yellow to blue, the picture is different. It witnesses values of η_{eq} and γ_{eq} both contained in the range $[0,1]$. In this zone, a balance between buoyancy-induced and wind-induced forces exist, providing the ideal conditions to appreciate the rich dynamical behaviour originated by the wind fluctuations. Recalling Figure 2.3, we notice that significant deviations of η_{eq} and γ_{eq} from unity are considerable in a wide range of the space of parameters. In particular, η_{eq} exhibits deviations from unity for all the considered values of V, which spans the range $[10^{-7},10^2]$.

On the contrary, γ_{eq} shows deviations from unity in a narrower range of V, namely for $V \gtrsim 10^{-4}$.

To conclude this analysis on the influence of V and W on η_{eq} and γ_{eq}, we discuss our results in terms of overshoot [Vesipa et al., 2023], recalling the analysis performed by Coomaraswamy and Caulfiled [2011]. They studied the deterministic transient dynamics of the interface height $\hat{h}(\hat{t})$ in Regime $\mathcal{A}$ from the condition $\hat{h}(\hat{t} = 0) = 1$ (i.e. a buoyant layer confined at the ceiling of the room) to the equilibrium condition $\hat{h}(\hat{t} \to \infty) = \hat{h}_0$. They found that the dynamics of $\hat{h}(\hat{t})$ exhibits an overshoot in the initial stages: the interface elevation $\hat{h}(\hat{t})$ suddenly decreases, reaching in some cases a minimum value $\hat{h}_{min}$ so that $\hat{h}_{min} < \hat{h}_0$; then, it rebounds and eventually it attains the equilibrium value $\hat{h}_0$. As done by Coomaraswamy and Caulfiled [2011] in their work, we map in Fig. 2.3 iso-lines of the difference $\hat{h}_0 - \hat{h}_{min}$ - the "overshoot size", as defined by Coomaraswamy and Caulfiled [2011]. It emerges a interesting fact: the portion of space parameters V, W in which the highest deviation from unity of η_{eq} are observed, is the same where the most relevant overshoots occur. This region of the space parameters appears to be the epicenter of a rich interplay of competing mechanisms, affecting the subtle balance between wind-induced and buoyancy-induced effects. When this balance is perturbed - by wind fluctuations in our case - the system responds amplifying disturbances. It results that when the system undergoes a continuous stochastic wind, the dynamical equilibrium configuration reached can be very different from the equilibrium attained in case of constant wind.

2.3   A real case study

In order to explain the utility of the study, let us show the effect of wind fluctuations on a real case study. Let us consider a conference room of height $H = 4m$ and cross sectional area $A_c = 50m^2$; such a room is similar to the room analysed by Lishman and Woods [2006]. The room presents two openings, one on the upwind face and one on the downwind face, with effective flow area equal to $A^* = 0.63m^2$. We consider inside the room a thermal load with power E=2000 W (such a power corresponds, e.g, to 13 people sitting around a table). From the thermal load a buoyancy flux arises, whose strength is $B_0 = g\beta \dfrac{E}{\rho c_p} = 4.13 \cdot 10^{-2} \ m^4 s^{-3}$, where $\beta = 5.50 \cdot 10^{-3} \ K^{-1}$ is the coefficient of thermal expansion and $c_p = 1012 \ J \ Kg^{-1} \ K^{-1}$ is the specific heat capacity. At the ceiling the reduced gravity reads $g'_H = 0.12 \ m/s^2$ (from Eq. 1.4). We consider a wind which blows at the mean velocity $v_0 = 1.40 \ m/s$, inducing a mean difference in pressure equal to $\Delta p_{w,0} = 1.22 \ Pa$, according to Eq. 1.6. Given this values of the parameters, by using Equations 1.3 and 1.7, we obtain $V = 1$ and $W = 2$, which are the cases shown in Figure 2.1. According to Eq. 1.24, the equilibrium configuration reached in Regime $\mathcal{A}$ is $\hat{h}_0 = 0.45$ and $\hat{g}_0 = 3.77$.

Firstly, we neglect wind fluctuations. It means that the room is affected by wind at a constant velocity $v_0 = 1.40 \ m/s$, inducing a reduced gravity within the buoyant layer $g' = 0.45 \ m/s^2$ and a interface elevation $h = 1.80 \ m$. It follows that people whose height is less than $1.80 \ m$ (which are the majority of people) breath below the buoyant layer.

Furthermore, considering an equilibrium condition for which $Q_B = Q_T = Q_P$, the flow rate of fresh air that enters in the room from the lower opening is equal to $Q_B = 0.12$ m^3/s (according to Equation 1.5), namely 2.1 air changes per hour.

Secondly, we take into account wind fluctuations. Considering coefficient of variation of the wind velocity equal to $C_{V,wv} = 0.10$, which is a reasonable assumption, we obtain as correction factors $\eta_{eq} \sim 0.6$ and $\gamma_{eq} \sim 0.8$, as shown in Figure 2.2. This way, the reduced gravity within the buoyant layer is $g' = 0.36$ m/s, the height of the interface is $h = 1.10$ m, the air exchange flow between the two layers is $Q_P = 0.05$ m^3/s, and only 0.9 air changes per hour occur. As we can notice, the situation for the salubrity of the air in the room have got worse compared to the case without wind fluctuations. Indeed, the room ventilation has dramatically changed. In this case, people breath air in the warm layer, implying

- less comfort, due to higher temperature and humidity,

- higher risk of mixing exhalations, which entails the spread of pathogens.

This example highlights the crucial impact of wind fluctuations on the natural ventilation of a room.

Chapter 3

Explanation of the phenomenon

In this section we intend to give an explanation of the phenomenon. In particular, we illustrate the reason why a stochastic perturbation with zero mean added to a constant wind alters the average dynamics of the system [Vesipa et al., 2023]. As we will show, it concerns a phenomenon of hysterisis.

In order to explain the physical reason of the phenomenon, we consider the response of the dynamical system to the presence of the wind parameter $W(t)$ which evolves as a periodic square wave. Such a behaviour is shown in Figure 3.1, and in particular the time series of $W(t)$ is reported in Fig. 3.1a. The square wave switches above and below the mean value W_0 of the same amount ΔW, keeping the values $W_0 + \Delta W$ and $W_0 - \Delta W$ for the same interval of time. Note that we consider a quantity ΔW such that $W_0 + \Delta W$ results beyond the bifurcation point: this way, a reverse flow (Regimes $\mathcal{B}$ and $\mathcal{C}$) can occur.

As shown in Figure 3.1, we assume that the system is initially in an equilibrium configuration of stratified forward flow, i.e. Regime $\mathcal{A}$, under the presence of a constant wind of strength W_0 (time interval $TI1$ in Fig. 3.1). Under this condition, recalling Equation 1.23, we note that the dimentionless buoyancy $\hat{B}$ is stronger than the wind parameter W: it means that buoyancy forces overcome wind forces, and thus the flow is expelled from the top opening, $Q_T > 0$ (as can be observed in Fig. 3.1b).

Things change when a change in the wind parameter W occurs. A different value of wind parameter W makes the system tends to a new equilibrium configuration, indeed. In case of an increment in the value of W, wind contrasts more the buoyancy effects of the warm layer; in this case, the new equilibrium configuration is characterized by lower h_0 and g_0. Conversely, in case of a decrease of W, wind can contrast less the buoyancy forces, resulting in an equilibrium configuration characterized by higher h_0 and g_0, as a stronger ejection of warm fluid from the top opening occurs.

43
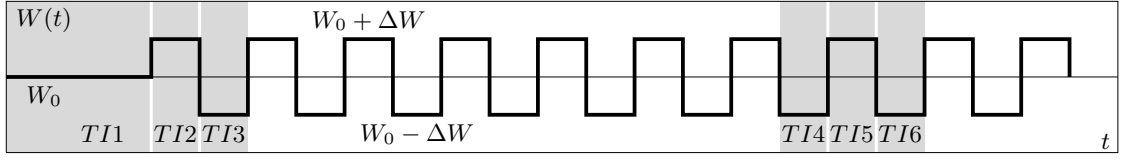
(a) Periodic square wave $W(t)$
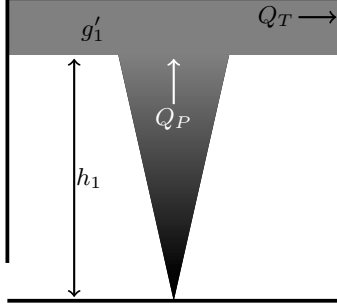
(b) Time interval $TI1$.
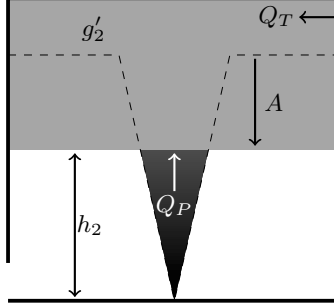
(c) Time interval $TI2$.
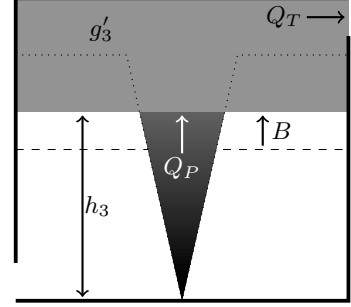
(d) Time interval $TI3$.
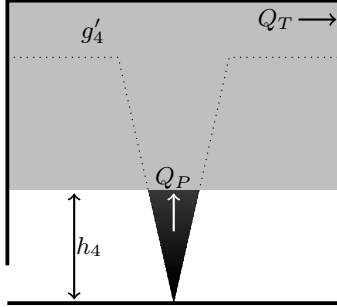
(e) Time interval $TI4$.
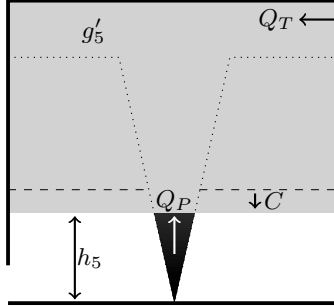
(f) Time interval $TI5$.
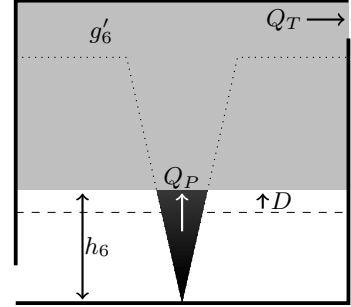
(g) Time interval $TI6$.

Figure 3.1: Schematic explanation of the physical mechanism which lead to a reduction of the average elevation of the interface between warm layer and cold layer h and the reduce gravity g'. For simplicity, the wind parameter $W(t)$ is taken as it evolves as a periodic square wave, as shown in 3.1a. Each plot represents a time interval, as explained by each caption. In each plot, the shaded area represents the system at the end of the time interval, the dashed line represents the configuration of the system at the beginning of the time interval, the dotted line represent the configuration of the system at the initial equilibrium, namely when the system undergoes a constant wind of strength $W(t) = W_0$. Vertical arrows show the direction and the magnitude of the displacement of the buoyant layer interface attained during the considered time interval. Different tone of gray are used: different gray intensities of the plume and of the warm layer denote difference air temperature. White is the coldest temperature considered (the temperature of the air outside); black is the hottest temperature (plume at the point source); intermediate temperature are rapresented by intermediate shades of gray.

Keeping in mind the possible responses that the system shows in case of changes of W, let us consider specifically the case in which the wind parameter $W(t)$ evolves as a periodic square wave, as shown in Fig. 3.1a.

At the beginning of the time interval $TI2$, an instantaneous switch of the value of

44

$W(t)$, from W_0 to $W_0 + \Delta W$, occurs. In this new configuration, the wind parameter is stronger than the buoyancy forces of the warm layer, i.e. $\hat{B} < W$ and $P < 0$. As a matter of fact, an imbalance between wind and buoyancy arises, and therefore the system tends to a new equilibrium for which the elevation of the interface between the two layers h has a lower value, so that the warm layer $H - h$ increases its depth (see the arrow A in Fig 3.1c). As $P < 0$, the cold ambient air enters from the top opening, namely $Q_T < 0$; this way, a reduction in g' occurs. Summing up, an increment in the value of $W(t)$ causes a strong reduction in the interface elevation h and the reduced gravity g' at the end of the time interval $TI2$, compared to the equilibrium state attained in the time interval $TI1$.

Now we shift the focus on the third time interval, $TI3$, where an instantaneous reduction of the wind parameter from the value $W_0 + \Delta W$ to $W_0 - \Delta W$ has occurred. Again, an imbalance between wind forces and buoyancy forces arises, this time in favour of buoyancy. Indeed, the system now tends to an equilibrium characterized by a thinner warm layer; therefore a modest increment of h occurs, as shown by the arrow B in Fig. 3.1d. During this time interval, the warm fluid is expelled from the top opening, $Q_T > 0$, and a stratified forward flow holds, resulting in a reduction of g'. As shown by the arrows A and B in Fig. 3.1c and 3.1d, respectively, during $TI3$ a smaller reduction of the buoyant layer thickness occurs, compared to the reduction achieved during $TI2$. The reason behind this behaviour lies in the fact that the cool air which enters from the top opening during $TI2$ causes a strong reduction of g'; conversely, the warm fluid provided by the plume during $TI3$ effects g' to a lesser extent, since its temperature is closer to the temperature of the warm fluid. This way, the increase of thickness of the warm layer during $TI3$ does not fully recover its reduction occurred during $TI2$. Summing up, at the end of $TI3$ an increment of the interface elevation h and the reduced gravity g' has occurred, but these increments is not strong enough to make the system reaches the initial equilibrium conditions. This way, the whole time interval formed by the pair $TI2 - TI3$ leads to a decreasing trend for both h and g'. This interplay between increasing and decreasing phase of $W(t)$ is the key which allows us to understand the decreasing trend of η and γ observed in Figure 2.1, for $\hat{t} \lesssim 2$.

We intend now to explain how a ventilated system eventually reaches a dynamic equilibrium (observed after the transient in Figure 2.1 for $\hat{t} \gtrsim 2$), under the presence of a fluctuating wind parameter $W(t)$. In order to do that, we conduct the same analysis already performed for $TI1$ ($W(t) = W_0$), $TI2$ ($W(t) = W_0 + \Delta W$) and $TI3$ ($W(t) = W_0 - \Delta W$), considering now the dynamic equilibrium condition which holds during $TI4$-$TI6$ (see Figures 3.1e-3.1g).
The time interval $TI4$ represents a condition of dynamical equilibrium. Its main features are:

(i) the interface elevation h of the warm layer is considerably lower than than the interface attained during the first time interval $TI1$ (compare in Figure 3.1e the elevation of the buoyant layer and the dotted line, which represents the initial equilibrium condition with constant wind during $TI1$);

(ii) the reduced gravity g'_4 of the warm layer is significantly lower than the reduced

45

gravity g'_1 at the top of the plume during $TI1$ (as represented by the different tones of gray in Fig. 3.1e and 3.1b).

Moving to the time intervals $TI5$ and $TI6$ we observe similar behaviour already noticed during $TI2$ and $TI3$. As in $TI2$, during $TI5$ the wind parameter $W(t)$ witnesses an increase in its value. Indeed, $W(t)$ increases from $W_0 - \Delta W$ to $W_0 + \Delta W$ and consequently:

(i) the thickness of the warm layer $H - h$ increases, as it can be observed by looking at the arrow C in Fig. 3.1f;

(ii) wind forces overcome buoyancy forces and cool ambient air enters from the top opening, i.e. $Q_T < 0$;

(iii) the reduced gravity reduces (note the difference tone of gray in Fig. 3.1f).

Conversely, as in $TI3$, during $TI6$ the wind parameter exhibits a reduction from $W_0 + \Delta W$ to $W_0 - \Delta W$. As a consequence we observe:

(i) the warm layer decreases, and similarly the buoyancy, resulting in an increment of h (see the arrow D in Fig. 3.1g);

(ii) buoyancy forces prevail on wind forces and re-establish a forward stratified flow, so that warm fluid overflows from the top opening ($Q_T > 0$);

(iii) g' increases once again.

However, there is a key difference between the dynamics occurring during $TI2$ and $TI5$, and those occurring during $TI3$ and $TI6$. The reduction of g' which is observed during $TI5$ is much smaller than the one attained during $TI2$, even if the system undergoes the same wind alteration which takes place for the same amount of time. The reason behind this behaviour lies in the difference of reduced gravity $\Delta g'_a$ between the buoyant layer and the cold ambient air. During $TI2$, this difference is high: since the system comes from a buoyancy-driven equilibrium, the warm fluid in the upper layer has not mixed before with cool ambient air. This implies that the inflow of a volume V_a of cold air reduced significantly the value of g' in the buoyant layer. Conversely, during $TI5$ the difference $\Delta g'_a$ is much lower than in $TI2$: in this case the fluid in the warm layer has already mixed with the cool ambient air, thus its temperature is lower than it was during $TI2$. As a result, the inflow of the same volume V_a of cold air reduces g' to a lesser extent.

A similar difference exists between $TI3$ and $TI6$: the increment in g' is much higher during $TI3$ than during $TI6$, indeed. Once again, the reason lies in a reduced gravity difference, this time between the warm layer and the plume, i.e. $\Delta g'_P$. During $TI3$ such a difference was small, because the warm layer affected by the plume had mixed with the cool air just for a small period of time. Therefore, the inflow of a volume V_P of warm fluid from the plume to the buoyant layer altered to a modest extent the reduced gravity g'. On the other hand, during $TI6$ $\Delta g'_P$ is much higher than in $TI3$, because in this case the upper layer has mixed with the ambient layer for a longer time. Consequently, the inflow of the same volume V_P of warm fluid from the plume induces an higher increment of reduced gravity g' in the buoyant layer.

Summing up:

(i) at the end of $TI5$ the interface elevation h and the reduced gravity g' have decreased compared to their value at the beginning of the time interval. However, such a reduction is lower than the one attained during $TI2$ (it can be noticed by comparing the size of the arrows C and A in Fig. 3.1f and 3.1c, respectively).

(ii) at the end of $TI6$ both h and g' have increased, reaching once again the same conditions attained during $TI4$. The increment witnessed by $TI6$ is lower than the one attained during $TI3$ (cfr. the sizes of the arrows D and B, respectively in Fig. 3.1g and 3.1d).

We can conclude that the system has reached a dynamical equilibrium: the elevation of the interface between the warm layer and the cool layer h and the reduced gravity g' keep oscillating around constant average values, which are lower than the ones attained in case of presence of a constant wind of strength W_0.

3.1 An analytical solution for the average values around which interface elevation h and reduced gravity g' oscillate

We intend now to give an analytical prediction for the mean values around which the height of the interface between the warm and cold layers h and the reduced gravity g' oscillate. In order to do that, we consider the case that we judge the most interesting: when the wind parameters $W(t)$ assumes values both preceding and beyond the bifurcation point, as already considered in the previous section (see Figure 3.1). This way, both forward and backward flows occur. To better understand the physical behaviour of the system, let us assume once again that the wind parameter $W(t)$ evolves as a periodic square wave around a mean value W_0, taking periodically values $W_0 + \Delta W$ and $W_0 - \Delta W$ for the same amount of time (as shown in Figure 3.1). In the previous section we have shown as under the presence of such a wind parameter, the system eventually reaches a dynamical equilibrium for which the elevation interface h and the reduced gravity g' keep oscillating around a pair of values, whose mean remains constant.

Recall that when a forward flow occurs (i.e. $Q_T > 0$, $P > 0$) Regime $\mathcal{A}$ is in force, while when a reverse flow occurs ($Q_T < 0$, $P < 0$) Regimes $\mathcal{B}$ and $\mathcal{C}$ are effective. Since in the considered case a reverse mixed flow is not attained, in the dynamical equilibrium Regimes $\mathcal{A}$ and $\mathcal{B}$ alternate. Such an alternation preserves a constant mean value around which h and g' oscillate if the temporal gradient of $h(t)$ ($g(t)$) when h (g) increases, namely when $W(t) = W_0 - \Delta W$ and thus Regime $\mathcal{A}$ occurs and $Q_T > 0$, is equal in magnitude and opposite in sign to the temporal gradient of $h(t)$ ($g(t)$) when $W(t) = W_0 + \Delta W$, and thus Regime $\mathcal{B}$ occurs, $Q_T < 0$ and h (g) decreases. Such a behaviour can be expressed by writing

$$\left(\frac{\mathrm{d}\hat{h}}{\mathrm{d}\hat{t}} \right)_{eq,up} = - \left(\frac{\mathrm{d}\hat{h}}{\mathrm{d}\hat{t}} \right)_{eq,down}, \tag{3.1a}$$

$$\left(\frac{\mathrm{d}\hat{g}}{\mathrm{d}\hat{t}}\right)_{eq,up} = -\left(\frac{\mathrm{d}\hat{g}}{\mathrm{d}\hat{t}}\right)_{eq,down}, \tag{3.1b}$$

$$\left(\frac{\mathrm{d}}{\mathrm{d}\hat{t}}[\hat{g}(1-\hat{h})]\right)_{eq,up} = -\left(\frac{\mathrm{d}}{\mathrm{d}\hat{t}}[\hat{g}(1-\hat{h})]\right)_{eq,down}, \tag{3.1c}$$

where the subscript *eq* indicates that they are the temporal gradients during the dynamical equilibrium, while the subscripts *up* and *down* specifies if the temporal gradient is referred to the ascent phase (Regime $\mathcal{A}$ is in force) or the descent phase (Regime $\mathcal{B}$ is effective), respectively. Recalling Equations 1.22, we can write the Equations 3.1 as

$$-\hat{h}^{5/3} + |VP_{eq,up}|^{1/2} = \hat{h}^{5/3} + |VP_{eq,down}|^{1/2}, \tag{3.2a}$$

$$1 - \hat{g}|VP_{eq,up}|^{1/2} = -1. \tag{3.2b}$$

Here $P_{eq,up}$ and $P_{eq,down}$ are defined as function of $\hat{h}_{eq}$ and $\hat{g}_{eq}$ (i.e. the mean values around which $\hat{h}$ and $\hat{g}$ oscillate, respectively) and $W_{up} = W_0 - \Delta W$ and $W_{down} = W_0 + \Delta W$, in the following way:

$$P_{eq,up} = \hat{g}_{eq}(1 - \hat{h}_{eq}) - W_{up}, \tag{3.3a}$$

$$P_{eq,down} = \hat{g}_{eq}(1 - \hat{h}_{eq}) - W_{down}. \tag{3.3b}$$

Solving the system given by the Equations 3.2 it is possible to find out the expected mean values around which $\hat{h}$ and $\hat{g}$ oscillate.

Note that strictly speaking, we consider and compute the temporal gradient at the midpoint of the ascent and descent phases. By doing so, we are performing an approximation: the temporal gradients in Equations 3.1 are not constant during the entire ascent and descent phases, but they slightly change. Such an approximation is justifiable by the fact that during the ascent and descent phase the temporal gradients vary regularly and linearly, assuming very close values. In order to legitimise this approximation we show in Figure FIG the behaviour of $\dfrac{\mathrm{d}\hat{h}}{\mathrm{d}\hat{t}}$ and $\dfrac{\mathrm{d}\hat{g}}{\mathrm{d}\hat{t}}$ in the $\hat{g} - \hat{h}$ space, in a specific case for which $V = 1$ and $W = 1.5$. Recall that our model holds only for the region under the curve $\hat{g} = \hat{h}^{5/3}$; furthermore, notice that for $P > 0$ a stratified forward flow occurs (Regime $\mathcal{A}$), while for $P < 0$ a reverse flow takes place (Regimes $\mathcal{B}$ or $\mathcal{C}$). By observing these plots, we remark that the trend of $\dfrac{\mathrm{d}\hat{h}}{\mathrm{d}\hat{t}}$ and $\dfrac{\mathrm{d}\hat{g}}{\mathrm{d}\hat{t}}$ is linear.

We expect that such an approximation depreciates as the duration of the temporal interval for which the wind parameter $W(t)$ keeps value $W_0 + \Delta W$ or $W_0 - \Delta W$ increases; if the time intervals are enough long, the system tends towards the steady states attained in case of constant wind, and thus the temporal gradients $\dfrac{\mathrm{d}\hat{h}}{\mathrm{d}\hat{t}}$ and $\dfrac{\mathrm{d}\hat{g}}{\mathrm{d}\hat{t}}$ tend to 0. In this case, the linear approximation does not hold anymore.

(a) $\frac{\mathrm{d}\hat{h}}{\mathrm{d}\hat{g}}$ (b) $\frac{\mathrm{d}\hat{g}}{\mathrm{d}\hat{t}}$
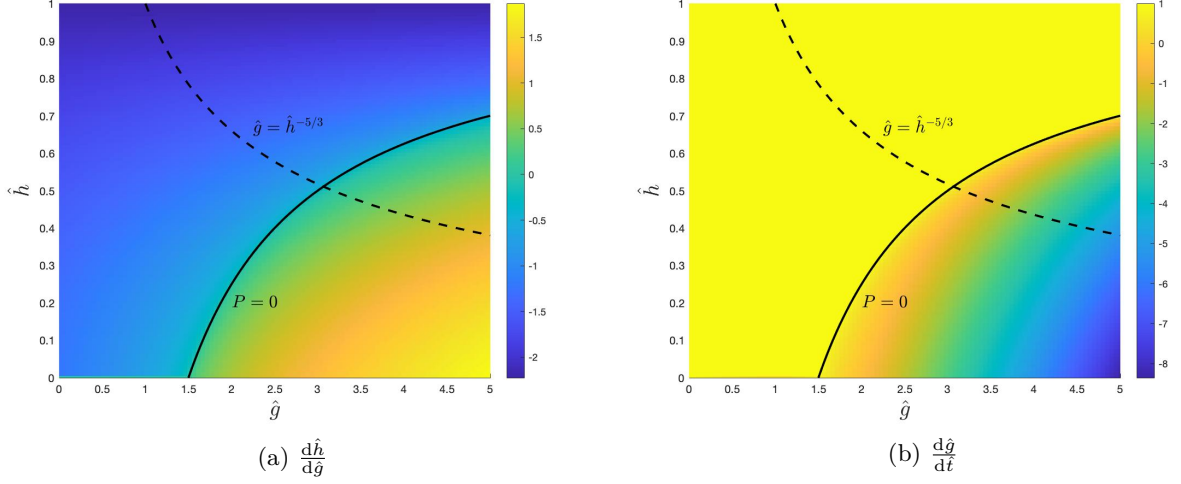
Figure 3.2: Magnitude of the temporal gradients of $\hat{h}(\hat{t})$ (3.2a) and $\hat{g}(\hat{t})$ (3.2b) computed for $V = 1$ and $W = 1.5$. Our model holds only for the region under the curve $\hat{g} = \hat{h}^{5/3}$. The curve $P = 0$ separate the region where forward flow occurs (on the right of the curve) and the region where reverse flow occurs (on the left of the curve).

3.1.1 Analytical prediction in case of stochastic fluctuations of $W(t)$

In case of stochastic fluctuations of the wind parameter $W(t)$, if the mean value W_0 is close enough to the bifurcation point, the system witnesses a high frequent switching straddling Regime $\mathcal{A}$ and $\mathcal{B}$.

In this case we can repeat the argument exposed above, to obtain a prediction for the mean values around which the height of the interface between the warm and cold layers h and the reduced gravity g' oscillate. Since the wind parameter $W(t)$ does not shift between just two values, we need to find a new definition for W_{up} and W_{down}. The old values can be replaced by the mean value of the PDF of $W(t)$ constrained to the bifurcation point. We expect also this approximation to work with reasonable accuracy.

3.2 Comparison with numerical simulations

Now we intend to validate the analytical solution for the average values around which the interface h and the reduced gravity g' oscillate, by performing some numerical simulations. As shown in the previous section, we consider a wind parameter $W(\hat{t})$ such that it assumes values preceding and beyond the bifurcation point. In particular, we first simulate the wind parameter $W(\hat{t})$ as it evolves as a square wave; then, we extend our validation to the case of stochastic fluctuations of $W(\hat{t})$.

3.2.1 $W(\hat{t})$ evolving as a square wave

In case of $W(\hat{t})$ evolving as a square wave, we first defined the wind parameter by setting $W_0 = 2$ and $\Delta W = 0.5$. This way we obtained a square wave which takes values $W(\hat{t}) = 2.5$ and $W(\hat{t}) = 1.5$ periodically. The period has been changed from simulation to simulation, in order to study how the dynamics of the system change when a different period occurs. The vent parameter V was set $V = 1$ for all the simulations. This way, by recalling that reverse flow can occur if $W^3 V > 27/4$, the bifurcation point is $W_{bif} = 1.8899$; the square wave is therefore straddling the bifurcation point.

Once defined the vent parameter $W(\hat{t})$, Equations 1.22 were solved to obtain the time series of the layer interface elevation $\hat{h}(\hat{t})$ and of the reduced gravity $\hat{g}(\hat{t})$. To compute that, the initial conditions $\hat{h}(\hat{t} = 0) = \hat{h}_0$ and $\hat{g}(\hat{t} = 0) = \hat{g}_0$ were set. Specifically, the values $\hat{h}_0$ and $\hat{g}_0$ correspond to the equilibrium configurations obtained from Eq. 1.24 (regime $\mathcal{A}$) setting $W = W_0$. Regarding the numerical integration, an explicit Runge-Kutta approach was used. Built-in MATLAB routines and functions (`ode45`) were used. The time duration of the simulations was set equal to $\hat{t} = 50$, so that $\hat{h}(\hat{t})$ and $\hat{g}(\hat{t})$ could reach the statistical steady state.

We report three different simulations which differ in the period of the wave square; in particular the considered periods are $\hat{T} = \frac{\pi}{5}, \frac{\pi}{4}, \pi$. In Figure 3.3 the time series of $W(\hat{t})$, $\hat{h}(\hat{t})$, $\hat{g}(\hat{t})$ and $\hat{g}(\hat{t})[1 - \hat{h}(\hat{t})]$ in these three different cases are shown. In the time series of the wind parameter $W(\hat{t})$ the dashed black line refers to the value of the bifurcation point; this way we can notice that the square wave is actually straddling it. In the time series of $\hat{h}(\hat{t})$, $\hat{g}(\hat{t})$ and $\hat{g}(\hat{t})[1 - \hat{h}(\hat{t})]$ the dotted red lines concern the initial conditions $\hat{h}_0$, $\hat{g}_0$ and $\hat{g}_0[1 - \hat{h}_0]$, which correspond to the equilibrium configuration when Regime $\mathcal{A}$ is in force and $W(\hat{t}) = W_0$; the dashed red lines refer to the expected values obtained by the system formed by Equations 3.2.

Firstly, we remark that during an initial transient - $0 < \hat{t} \lesssim 4$ - both $\hat{h}$ and $\hat{g}$ reduce significantly, reaching a dynamic equilibrium around which they keep oscillating for $\hat{t} \gtrsim 4$. For periods $\hat{T} = \frac{\pi}{5}, \frac{\pi}{4}$, the mean values around which $\hat{h}$ and $\hat{g}$ fluctuate are in accordance with the solutions of the system given by Equations 3.2, as we can see by looking at the dashed red lines in the Figures 3.3d,3.3e and 3.3g,3.3h. As the period of the square wave that governs the wind parameter $W(\hat{t})$ increases, the approximation of the mean values of $\hat{h}$ and $\hat{g}$ worsens (Figures 3.3f and 3.3i).

Secondly, we focus on the behaviour of $\hat{g}[1 - \hat{h}]$, which is the dimensionless buoyancy $\hat{B}$ in the warm layer. Recalling Equations 1.23, we can understand the resulting balance between the competing effects of wind and buoyancy by remarking which values $\hat{B}$ assumes: if $\hat{B} > W$ buoyancy forces are stronger than wind strength, resulting in a buoyancy-driven forward flow; if $\hat{B} < W$ wind strength is predominant on buoyancy forces and a wind-driven reverse flow occurs. As it can be observed in Figures 3.3j-3.3l, the expected value is $\hat{g}_0[1 - \hat{h}_0] \simeq W_0$: during the dynamical equilibrium we foresee that a balance between buoyancy and wind exists, such that their effects compensate. Thus,

since the wind parameter fluctuates around W_0, it is reasonable to imagine that also $\hat{B}$ has to oscillate around W_0. Such a balance vanishes for $\hat{T} = \pi$: as can be observed in Figure 3.3l, in this case $\hat{g}[1 - \hat{h}]$ takes lower values, thus its mean is lower than W_0. It means that buoyancy forces are dominated by wind effects. In this case the prediction of $\hat{h}$ and $\hat{g}$ given by Equations 3.2 is not reliable anymore, as already observed by looking at the behaviours of $\hat{h}$ and $\hat{g}$.

Thirdly, we make an additional consideration regarding the dynamics of the system conforming to the analytical prediction discussed in the previous section. The system given by Equations 3.2 takes into account an alternation between the Regimes $\mathcal{A}$ and $\mathcal{B}$. As the period of the square wave increases, the system tends toward the steady states attained in case of constant wind, i.e. the steady states governed by either Regime $\mathcal{A}$ or Regime $\mathcal{C}$. Therefore, in order to predict the mean values around which $\hat{h}$ and $\hat{g}$ fluctuate we should take into account all the three Regimes; thus an equivalence between the temporal gradients in Regimes $\mathcal{A}$ and $\mathcal{B}$ is not sufficient. Furthermore, as already mentioned in the previous section, if the system has enough time to tend to the steady states proper to the case of constant wind, the temporal gradients $\frac{d\hat{h}}{d\hat{t}}$ and $\frac{d\hat{g}}{d\hat{t}}$ tend to 0; in this case, the linear approximation is not valid anymore. In Figure 3.4, the temporal gradients $\frac{d\hat{h}}{d\hat{t}}$ during the dynamical equilibrium for $\hat{T} = \frac{\pi}{5}$ (Fig. 3.4a) and $\hat{T} = \pi$ (Fig. 3.4b) are reported. As we can observe, the linear approximation is valid if the period is short enough ($\hat{T} = \frac{\pi}{5}$), while it loses its validity as the period increases ($\hat{T} = \pi$).

In order to better understand the dynamics of the system and to better comprehend between which states the variables $\hat{h}$ and $\hat{g}$ fluctuate around, it is useful to study their distribution by looking at their probability density function. In Figure 3.5, PDFs of the interface elevation $\hat{h}$ and the reduced gravity $\hat{g}$ during the dynamical equilibrium for all the periods considered are reported: in the first row a comparison between the PDFs of $\hat{h}$ is shown, while in the second row the PDFs of $\hat{g}$ are displayed. In all the figures it is reported the expected values around which $\hat{h}$ and $\hat{g}$ fluctuate (black dotted line); moreover, the steady stable states driven by Regime $\mathcal{A}$ (red dashed line) and Regime $\mathcal{C}$ (blue dashed line) when the wind parameter $W(\hat{t})$ is constant and equal to $W_0 = 2$ are shown.

As it can be observed by looking at Fig. 3.5a and 3.5d, when the period of the wave square governing the wind parameter is short, the PDFs of $\hat{h}$ and $\hat{g}$ during the dynamical equilibrium are bimodal and the picks straddle the expected mean value: the interface elevation and the reduced gravity keep switching between two values whose average coincides with the solution of system given by Eq. 3.2, indeed. This means that the analytical solution works and the system is governed by Regimes $\mathcal{A}$ and $\mathcal{B}$ as we expect. Note that both the two picks correspond to values of $\hat{h}$ and $\hat{g}$ are lower than steady buoyancy-driven state in case of constant wind parameter $W(\hat{t}) = W_0 = 2$, as already observed in the time series; on the other hand, Regime $\mathcal{C}$ never occurs, as can be noticed from the fact that the interface never reaches the ground, i.e. $\hat{h}$ is never equal to 0.

As the period of the wave square governing $W(\hat{t})$ increases, the two picks of the PDFs

of $\hat{h}$ and $\hat{g}$ distance from each other and become smoother, as can be observed by looking at Fig. 3.5b and 3.5e. This behaviour is due to the fact that as the time interval for which $W(\hat{t})$ keeps constant value increases, the system has more time to tend towards its steady states proper to Regimes $\mathcal{A}$ and $\mathcal{C}$, and thus the two values between which $\hat{h}$ and $\hat{g}$ oscillate are more distant. The values of $\hat{h}$ and $\hat{g}$ reached during the ascent phase are still lower than the steady state proper to buoyancy-driven Regime $\mathcal{A}$, but the distance has decreased with respect to case for which the period is $\hat{T} = \frac{\pi}{5}$. Moreover, both the interface elevation and the reduced gravity take more intermediate values, which explains the reason why the picks of the PDFs are smoother. Note that in the considered case - for which the period is $\hat{T} = \frac{\pi}{4}$ - the analytical prediction for the mean value of $\hat{h}$ and $\hat{g}$ is still valid, as can be remarked by looking at the black dotted line in Fig. 3.5b and 3.5e; furthermore, the interface between the warm and cold layers still does not reach the ground, and thus Regime $\mathcal{C}$ still does not occur.

If the period increases again - $\hat{T} = \pi$ as reported in Fig. 3.5c and 3.5f - the situation changes. In this case the PDFs of both $\hat{h}$ and $\hat{g}$ are not bimodal anymore and they take value in a wider range. Indeed the system has more time to reach the steady states proper to either buoyancy-driven or wind-driven configuration, and it assumes all the intermediate values. It is the reason why the PDF of $\hat{g}$ exhibits an intermediate pick between the picks relative to the two values between which the reduced gravity oscillates, and why the PDF of $\hat{h}$ has several picks; note that the PDF of the interface elevation has just one remarkable pick, which is relative to $\hat{h} = 0$: it is due the fact that when the interface descends to the ground it cannot but takes value $\hat{h} = 0$, while when it ascend toward the steady state proper to buoyancy-driven configuration, it can assumes values which differ for small differences. As already mentioned, in this case Regime $\mathcal{C}$ occurs and thus the analytic prediction for the mean value of $\hat{h}$ and $\hat{g}$ given by Equations 3.2 is not accurate anymore; this fact is prominent in the PDF of the reduced gravity. Regarding the steady stable state proper to Regimes $\mathcal{A}$ and $\mathcal{C}$ when $W(\hat{t}) = 2$ (red dashed line and blue dotted line, respectively), we see that in this case the system approaches them: the interface height reaches the ground and almost the buoyancy-driven steady state; the reduced gravity still does not reach them but it comes significantly closer than in case of period equal to $\hat{T} = \frac{\pi}{5}$ or $\hat{T} = \frac{\pi}{4}$.

It is possible to make an additional consideration about the PDFs by looking at statistical moments of the time series of $\hat{h}$ and $\hat{g}$. In particular, we report in Table 3.1 the first four statistical moments of the interface level and the reduced gravity, for the considered periods.

Firstly, we report the expected mean values of $\hat{h}$ and $\hat{g}$ - which we rename as $\hat{h}_{eq}$ and $\hat{g}_{eq}$, respectively - obtained by the system given by Equations 3.2 by substituting $W_{up} = 1.5$ and $W_{down} = 2.5$ in the definition of P_{up} and P_{down} (Equations 3.3):

$$\hat{h}_{eq} = 0.1956, \quad \hat{g}_{eq} = 2.6016; \tag{3.4}$$

then, the mean value of $\hat{h}$ and $\hat{g}$ when the period of the square wave is $\hat{T} = \frac{\pi}{5}$ or $\hat{T} = \frac{\pi}{4}$ is in good agreement with the analytical prediction. As the period increases, i.e. for $\hat{T} = \pi$, the accuracy of the analytical solution for the averaged value of the interface level and

	$\hat{T} = \frac{\pi}{5}$	$\hat{T} = \frac{\pi}{4}$	$\hat{T} = \pi$
mean of $\hat{h}$	0.1836	0.18020	0.0922
variance of $\hat{h}$	0.0061	0.0077	0.0239
skewness of $\hat{h}$	0.3317	0.4406	1.4923
kurtosis of $\hat{h}$	1.8142	2.1569	3.7250
mean of $\hat{g}$	2.5961	2.6396	2.1964
variance of $\hat{g}$	0.0201	0.0252	0.1856
skewness of $\hat{g}$	1.8979	1.7408	1.6329
kurtosis of $\hat{g}$	10.7285	8.9042	6.2731

Table 3.1: Statistical moments of $\hat{h}$ and $\hat{g}$ when $W(\hat{t})$ evolves as a square wave of period $\hat{T} = \frac{\pi}{5}, \frac{\pi}{4}, \pi$.

the reduced gravity decreases, and the mean of $\hat{h}$ and $\hat{g}$ deviates.

Secondly, as we expect, the variance of the distribution of both $\hat{h}$ and $\hat{g}$ increases as the period of the square wave $\hat{T}$ increases. When the period is greater, the system has more time to tend towards the steady states, thus the interface level and the reduced gravity oscillate across a wider range, indeed. We notice that the variance in case of $\hat{T} = \frac{\pi}{5}$ and $\hat{T} = \frac{\pi}{4}$ is comparable, whereas when $\hat{T} = \pi$ it increases considerably.

Thirdly, regarding the third standardized moment, which is the skewness, it can be noticed that as the period of the square wave $\hat{T}$ increases, it increases for the distribution of $\hat{h}$, whereas it decreases for the distribution of $\hat{g}$. Furthermore, for all the distributions considered, the skewness is positive, highlighting that the tail of the distributions is longer on the right. These behaviours can be explained recalling that, regarding the height of the interface $\hat{h}$, its PDF changes from a bimodal distribution to a distribution presenting one great pick on the left (which corresponds to $\hat{h}$ taking value 0) and several much smaller picks on the right. On the other hand, the distribution of $\hat{g}$ is at first bimodal when $\hat{T} = \frac{\pi}{5}$, whereas for $\hat{T} = \pi$ it presents a major pick between the values corresponding to the steady states which the system tends towards, thus we can say that its tail reduces.

Fourthly, we consider the standardized fourth moment, the kurtosis. As the skewness, it increases for the distributions of $\hat{h}$ when the period of the square wave increases, and it decreases for the distributions of $\hat{g}$ as $\hat{T}$ increases. Furthermore it assumes much higher values for $\hat{g}$ than for $\hat{h}$. Recalling that the kurtosis is a measure of the heaviness of the tail of the distribution, the same arguments made regarding the skewness apply. We can make just an additional observation, by noticing that the values of the kurtosis regarding $\hat{g}$ are much higher than those relative to $\hat{h}$: it can be explained by observing that the tails of the distributions of $\hat{g}$ correspond to the picks relative to steady states which the system tends towards, and thus they are heavier.

3.2.2 $W(\hat{t})$ forced by a stochastic wind velocity

In order to validate the analytical prediction for the average values around which the interface h and the reduced gravity g' fluctuate in case of stochastic wind parameter $W(\hat{t})$,

we performed some numerical simulation as already explained in the previous chapter. We recall that in case of stochastic wind velocity, we substitute W_{up} and W_{down} in the definitions of $P_{eq,up}$ and $P_{eq,down}$ in Eq. 3.2 with the mean value of the PDF of $W(\hat{t})$ before and beyond the bifurcation point.

Firstly, we set the vent parameter, which has been chosen $V = 1$, and the wind characteristics (i.e. the mean wind W_0 and the fluctuations properties, $\hat{\tau}_{wv}$ and $C_{V,wv}$). In particular, since we are interested in time series of the wind parameter in which $W(\hat{t})$ straddles the bifurcation point, we considered the mean wind $W_0 = 1.5, 2, 2.5$. Recalling what we have observed in the previous chapter , since changes in the relaxation time $\hat{\tau}_{wv}$ have a limited influence on the dynamics of the system, we have taken into account just one value, i.e. $\hat{\tau}_{wv} = 0.1$. On the other hand, regarding the coefficient of variation of the wind velocity $C_{V,wv}$, we have considered three different values: $C_{V,wv} = 0.05, 0.1, 0.15$. Once the wind characteristics and the vent parameter have been set, the time series of the wind velocity fluctuations was simulated according to 2.4, and thus the corresponding time series of the wind parameter $W(\hat{t})$ was computed using 2.9. Note that the same series of random numbers n was maintained in order to keep the results comparable (thus the simulations differ for the values of $V, W_0, \hat{\tau}_{wv}, C_{V,wv}$).

Secondly, equations 1.22 were forced with $W(\hat{t})$ and numerically solved in order to obtain the time series of the layer interface elevation $\hat{h}(\hat{t})$ and of the reduced gravity $\hat{g}(\hat{t})$. To compute that, the initial conditions $\hat{h}(\hat{t} = 0) = \hat{h}_0$ and $\hat{g}(\hat{t} = 0) = \hat{g}_0$ were set. Specifically, the values $\hat{h}_0$ and $\hat{g}_0$ correspond to the equilibrium configurations obtained from eq. 1.24 (regime $\mathcal{A}$) setting $W(\hat{t}) = W_0$. Once again, to compute the numerical integration, an explicit Runge-Kutta approach was used. Built-in MATLAB routines and functions (`ode45`) were used. The time duration of the simulations was set equal to $4000\tau_{wv}$, so that $\hat{h}(\hat{t})$ and $\hat{g}(\hat{t})$ could reach the statistical steady state.

We report the time series of the wind parameter $W(\hat{t})$, their relative time series of $\hat{h}(\hat{t})$, $\hat{g}(\hat{t})$, and the distribution of $\hat{h}(\hat{t})$, $\hat{g}(\hat{t})$, for each considered combination of wind characteristics. In Figure 3.6 the different cases regarding $W_0 = 1.5$ are shown; in Figure 3.7 all the time series and the PDFs related to $W_0 = 2$ are reported; Figure 3.8 corresponds to the case for which $W_0 = 2.5$. In all the Fig. 3.6, 3.7, 3.8, the first column refers to $C_{V,wv} = 0.05$, the second to $C_{V,wv} = 0.1$, the third to $C_{V,wv} = 0.15$. In the plots of the time series of $W(\hat{t})$ the black dashed lines refer to the bifurcation point; in the time series of $\hat{h}(\hat{t})$ and $\hat{g}(\hat{t})$, the red dotted lines correspond to the initial values (solutions of Eq. 1.24, namely the steady solution when Regime $\mathcal{A}$ is in force and $W(\hat{t}) = W_0$) and the red dashed lines refer to the expected values $\hat{h}_{eq}$ and $\hat{g}_{eq}$ obtained from the system given by Equations 3.2; in the PDFs of $\hat{h}$ and $\hat{g}$, the black dotted lines refer to $\hat{h}_{eq}$ and $\hat{g}_{eq}$, respectively, the red dashed lines to the solution of Eq. 1.24 (steady state when Regime $\mathcal{A}$ is in force) when $W(\hat{t}) = W_{up}$, the blue dashed lines to the steady solution of 1.25 (stable steady state when Regime $\mathcal{C}$ is in force) when $W(\hat{t}) = W_{down}$.

Moreover, in Table 3.2 the expected values $\hat{h}_{eq}$, $\hat{g}_{eq}$ and the first four statistical moments of each time series are reported.

Firstly, we consider $W_0 = 1.5$. When the coefficient of variation of the wind velocity

$C_{V,wv}$ is low, i.e. $C_{V,wv} = 0.05$, the wind parameter $W(\hat{t})$ assumes value lower than the bifurcation point at almost every moment (see Fig. 3.6a); this means that the forward flow is almost always maintained in the time series. Such a behaviour is remarkable by looking at the behaviour of $\hat{h}$ (Fig. 3.6d): the mean value of the oscillations of the interface elevation is approximately equal to the initial condition. By looking at the PDFs of $\hat{h}$ (Fig. 3.6j), we observe that the pick is around the steady state when Regime $\mathcal{A}$ is in force. As the coefficient of variation of the wind velocity $C_{V,wv}$ increases, the wind parameter $W(\hat{t})$ assumes more values beyond the critical point: this way, reverse flow occurs. The occurrence of reverse flow causes a reduction of the mean value around which $\hat{h}$ fluctuates (see Fig. 3.6e, 3.6f), and the prediction given by Eq. 3.2 improves (cfr. the picks in Fig. 3.6k, 3.6l with the black dotted lines). Such improvement is remarkable also by looking at the mean value reported in Table 3.2; moreover, as we expect, as $C_{V,wv}$ increases, the amplitude of the oscillation enlarges and the variance of $\hat{h}$ increases. Regarding the reduced gravity $\hat{g}$, we notice that the expected value obtained from Eq. 3.2 is accurate for each value of $C_{V,wv}$ (see the red dashed lines in Fig. 3.6g, 3.6h, 3.6i and compare the picks of the PDFs with the black dotted lines in Fig. 3.6m, 3.6n, 3.6o). As already observed for $\hat{h}$, as the coefficient of variation of the wind velocity increases, the mean value around which $\hat{g}$ fluctuates decreases, and the amplitude of the oscillations enlarges (cfr. Table 3.2).

Secondly, we investigate the behaviour of the system when $W_0 = 2$. In this case, for any value of the coefficient of variation of the wind velocity $C_{V,wv}$, the wind parameter $W(\hat{t})$ straddles the bifurcation value. Therefore, alternation between forward and reverse flow occurs continuously. Such an alternation causes a reduction of the mean value of both $\hat{h}$ and $\hat{g}$, in accordance with what expected; furthermore, the analytical predictions $\hat{h}_{eq}$ and $\hat{g}_{eq}$ are accurate (see the red dashed lines reported in the time series of $\hat{h}$ - Fig. 3.7d, 3.7e, 3.7f - and $\hat{g}$ - Fig. 3.7g, 3.7h, 3.7i - and the picks of their PDFs - Fig. 3.7m, 3.7n, 3.7o and Fig. 3.7j, 3.7k, 3.7l). Note that when $C_{V,wv} = 0.15$ the oscillations of the wind parameter are larger, resulting in higher oscillations of $\hat{h}$ and $\hat{g}$ (cfr. the variances reported in Table 3.2) and in higher values reached by $W(\hat{t})$; such values lead the system to be driven by Regime $\mathcal{C}$, i.e. they lead the elevation interface $\hat{h}$ to reach 0. This fact is remarkable in the PDF of $\hat{h}$ (see Fig. 3.7l): the major pick is in correspondence to the value 0, while the expected value $\hat{h}_{eq}$ exhibits a lower pick. Such a shape of the PDF is noticeable also by considering the sign of the skewness (cfr. Table 3.2): contrary to the cases of lower $C_{V,wv}$, when $C_{V,wv} = 0.15$ the skewness is positive, resulting in a different asymmetry of the PDF. The interface elevation $\hat{h}$ reaching 0 implies the worsening of the analytical prediction, as can be observed by comparing $\hat{h}_{eq}$ and the mean value of $\hat{h}$ in Table 3.2. As already mentioned, the system given by Eq. 3.2 does not take into account Regime $\mathcal{C}$, indeed.

Thirdly, we consider $W_0 = 2.5$. Contrary to the case for which $W_0 = 1.5$, when $W_0 = 2.5$ the wind parameter is almost always beyond the bifurcation condition, resulting in a change of the dynamics of the system. For low value of the coefficient of variation of the wind velocity, i.e. $C_{V,wv} = 0.05$, we observe a reduction in the mean value of both $\hat{h}$ and $\hat{g}$ as observed in the previous cases. Contrary to the previous cases, the analytical

prediction for the mean value of $\hat{h}$ and $\hat{g}$ is not accurate (see red dashed lines in Fig. 3.8d, 3.8g, the picks of the PDFs in Fig. 3.8j, 3.8m, and compare $\hat{h}_{eq}$ and $\hat{g}_{eq}$ with the mean of $\hat{h}$ and $\hat{g}$ in Table 3.2). Such a difference is attributable to the fact that since the wind parameter is almost always beyond the bifurcation point, Regime $\mathcal{A}$ - i.e. forward flow - never occurs. By observing that the elevation interface $\hat{h}$ does not reach 0, we can deduce that the system has reached a dynamical equilibrium driven by Regime $\mathcal{B}$; note that under deterministic conditions, Regime $\mathcal{B}$ is purely transient, and steady solutions in Regime $\mathcal{B}$ do not exist. The picture changes when $C_{V,wv}$ increases. As the amplitude of the oscillations of $W(\hat{t})$ enlarges, wind forces become too strong, overcoming the buoyancy forces and leading the systems to be driven just by Regime $\mathcal{C}$. Indeed, $\hat{h}$ reaches 0, while the values assumed by $\hat{g}$ coincide to the stable state solutions of Equation 1.25, which are proper to Regime $\mathcal{C}$. Such a behaviour is remarkable by looking at the PDFs of both $\hat{h}$ and $\hat{g}$ (see Fig. 3.8k, 3.8l and 3.8n, 3.8o): the picks of the PDFs are in correspondence to the blue dashed line, i.e. the steady solution of 1.25 when $W(\hat{t}) = W_{down}$. Note that when $C_{V,wv} = 0.1$, Regime $\mathcal{B}$ is preserved for a short time, namely until $\hat{t} \lesssim 40$ (see Fig. 3.8e and 3.8h); on the contrary, when $C_{V,wv} = 0.15$, Regime $\mathcal{C}$ immediately occurs (cfr. Fig. 3.8f and 3.8i).

	$W_0 = 1.5, C_{V,wv} = 0.05$	$W_0 = 1.5, C_{V,wv} = 0.1$	$W_0 = 1.5, C_{V,wv} = 0.15$
exp. val. $\hat{h}_{eq}$	0.3961	0.3356	0.2770
mean of $\hat{h}$	0.4725	0.4119	0.3474
variance of $\hat{h}$	0.0011	0.0046	0.0109
skewness of $\hat{h}$	-0.5001	-0.3836	-0.3983
kurtosis of $\hat{h}$	3.3046	3.0070	2.8876
exp. val. $\hat{g}_{eq}$	3.1496	2.8954	2.6634
mean of $\hat{g}$	3.1008	2.8492	2.6230
variance of $\hat{g}$	0.0090	0.0300	0.0508
skewness of $\hat{g}$	-0.7573	-0.6251	-0.4847
kurtosis of $\hat{g}$	4.1429	3.3965	3.0561
	$W_0 = 2, C_{V,wv} = 0.05$	$W_0 = 2, C_{V,wv} = 0.1$	$W_0 = 2, C_{V,wv} = 0.15$
exp. val. $\hat{h}_{eq}$	0.4126	0.2918	0.2107
mean of $\hat{h}$	0.3887	0.2829	0.1537
variance of $\hat{h}$	0.0021	0.0099	0.0166
skewness of $\hat{h}$	-0.4171	-0.4176	0.5194
kurtosis of $\hat{h}$	3.1181	2.9626	2.2867
exp. val. $\hat{g}_{eq}$	3.5567	2.9538	2.6354
mean of $\hat{g}$	3.4623	3.0125	2.5599
variance of $\hat{g}$	0.0194	0.0561	0.09843
skewness of $\hat{g}$	-0.6689	-0.4291	-0.1700
kurtosis of $\hat{g}$	3.54019	2.9384	2.7718
	$W_0 = 2.5, C_{V,wv} = 0.05$	$W_0 = 2.5, C_{V,wv} = 0.1$	$W_0 = 2.5, C_{V,wv} = 0.15$
exp. val. $\hat{h}_{eq}$	0.2424	0.1832	0.1054
mean of $\hat{h}$	0.3030	0.0584	0.0032
variance of $\hat{h}$	0.0037	0.0101	0.0000
skewness of $\hat{h}$	-0.40771	1.7391	11.2337
kurtosis of $\hat{h}$	3.0705	5.0377	133.0108
exp. val. $\hat{g}_{eq}$	3.0091	2.7443	2.4809
mean of $\hat{g}$	3.7300	1.7285	0.8343
variance of $\hat{g}$	0.0363	1.2662	0.0910
skewness of $\hat{g}$	-0.5439	0.4069	7.6977
kurtosis of $\hat{g}$	3.4732	1.3438	70.8389

Table 3.2: Statistical moments and expected values of $\hat{h}$ and $\hat{g}$ when $W(\hat{t})$ is forced by a stochastic wind velocity, whose characteristic are $W_0 = 1.5, 2, 2.5$, $\hat{\tau}_{wv} = 0.1$ and $C_{V,wv} = 0.05, 0.1, 0.15$. The vent parameter is fixed, $V = 1$.

(a) $\hat{T} = \frac{\pi}{5}$

(b) $\hat{T} = \frac{\pi}{4}$

(c) $\hat{T} = \pi$

(d) $\hat{T} = \frac{\pi}{5}$

(e) $\hat{T} = \frac{\pi}{4}$

(f) $\hat{T} = \pi$

(g) $\hat{T} = \frac{\pi}{5}$

(h) $\hat{T} = \frac{\pi}{4}$

(i) $\hat{T} = \pi$

(j) $\hat{T} = \frac{\pi}{5}$

(k) $\hat{T} = \frac{\pi}{4}$

(l) $\hat{T} = \pi$
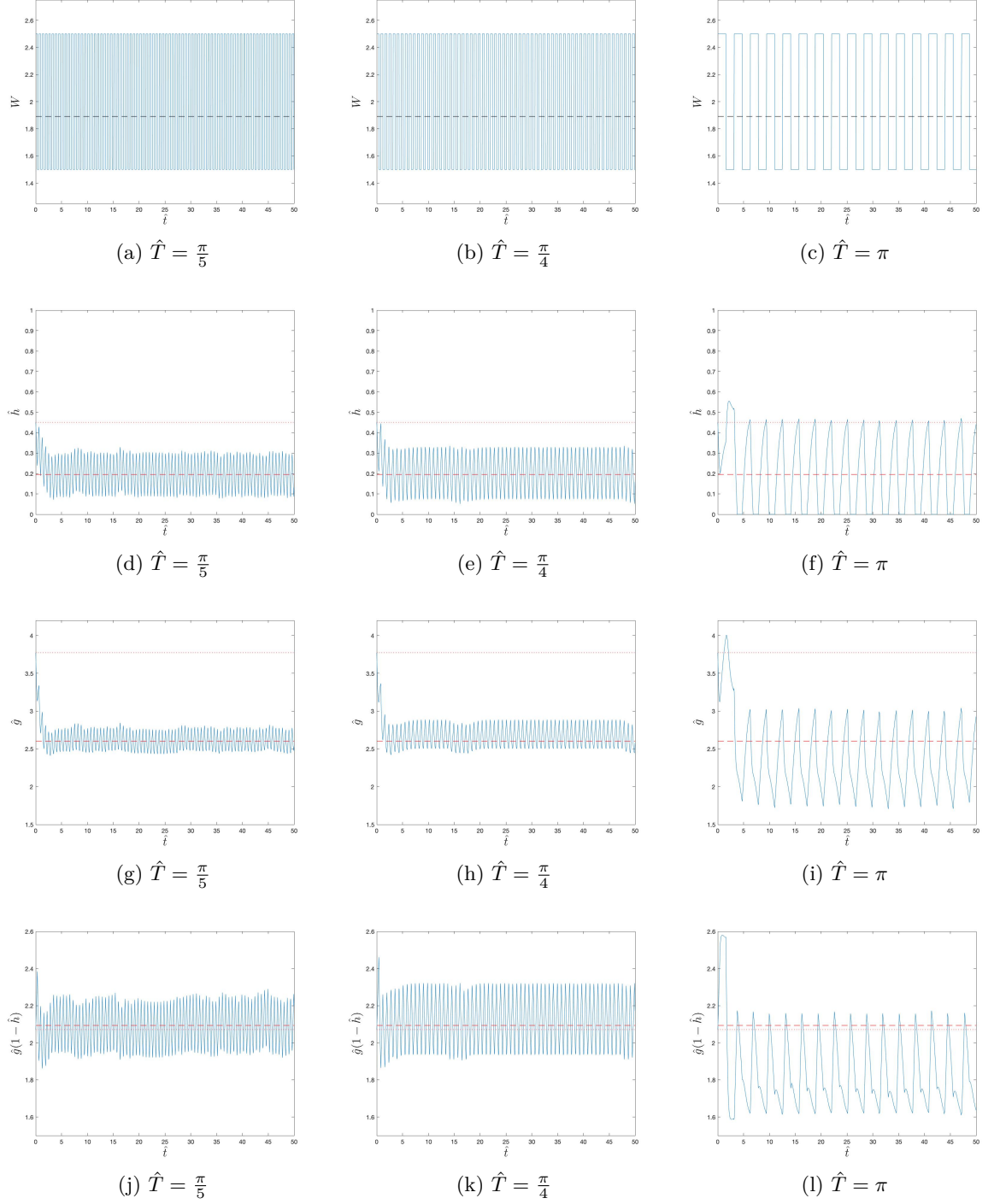
Figure 3.3: Time series of the wind parameter $W(\hat{t})$ evolving as a square wave taking values $W_0 + \Delta W = 2.5$ and $W_0 - \Delta W = 1.5$ (first row - 3.3a,3.3b,3.3c) when the periods are $\hat{T} = \frac{\pi}{5}, \frac{\pi}{4}, \pi$, respectively. The dashed black line refers to the value of the bifurcation point. For all the simulations, $V = 1$ was considered. Below every time series of $W(\hat{t})$, the respective time series of $\hat{h}(\hat{t})$, $\hat{g}(\hat{t})$ and $\hat{g}(\hat{t})[1 - \hat{h}(\hat{t})]$ are reported, respectively. In these time series, the dotted red lines concern the initial conditions $\hat{h}_0$, $\hat{g}_0$ and $\hat{g}_0[1 - \hat{h}_0]$, which correspond to the equilibrium configuration when Regime $\mathcal{A}$ is in force and $W(\hat{t}) = W_0$; the dashed red lines refer to the expected values obtained by the system formed by Equations 3.2.
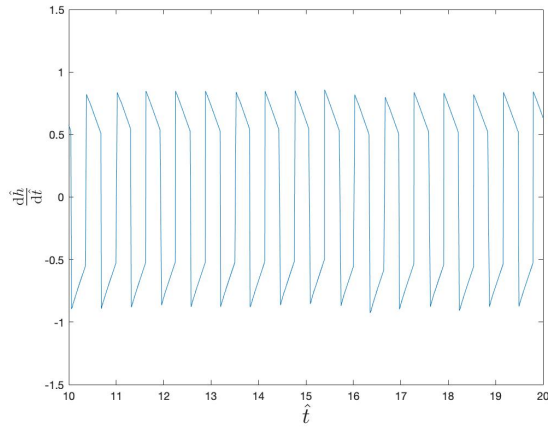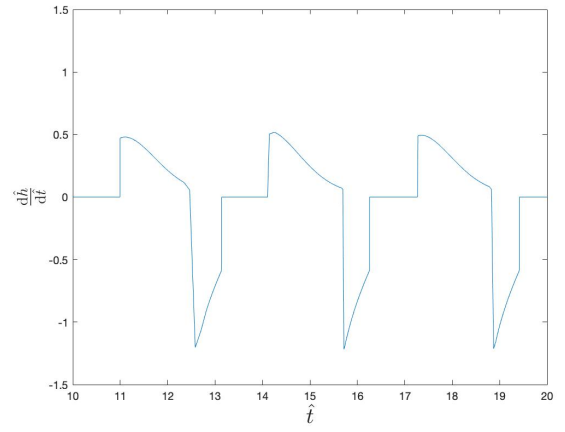
(a) $\hat{T} = \frac{\pi}{5}$ (b) $\hat{T} = \pi$

Figure 3.4: Temporal gradients $\frac{\mathrm{d}\hat{h}}{\mathrm{d}\hat{t}}$ during the dynamical equilibrium when $\hat{T} = \frac{\pi}{5}$ (3.4a) and $\hat{T} = \pi$ (3.4b). If $\hat{T} = \frac{\pi}{5}$ the linear approximation of temporal gradient of $\hat{h}(\hat{t})$ is valid; when $\hat{T} = \pi$ does not hold and the temporal gradient takes value 0.

59

(a) PDF of $\hat{h}$ when $\hat{T} = \frac{\pi}{5}$

(b) PDF of $\hat{h}$ when $\hat{T} = \frac{\pi}{4}$

(c) PDF of $\hat{h}$ when $\hat{T} = \pi$

(d) PDF of $\hat{g}$ when $\hat{T} = \frac{\pi}{5}$

(e) PDF of $\hat{g}$ when $\hat{T} = \frac{\pi}{4}$

(f) PDF of $\hat{g}$ when $\hat{T} = \pi$
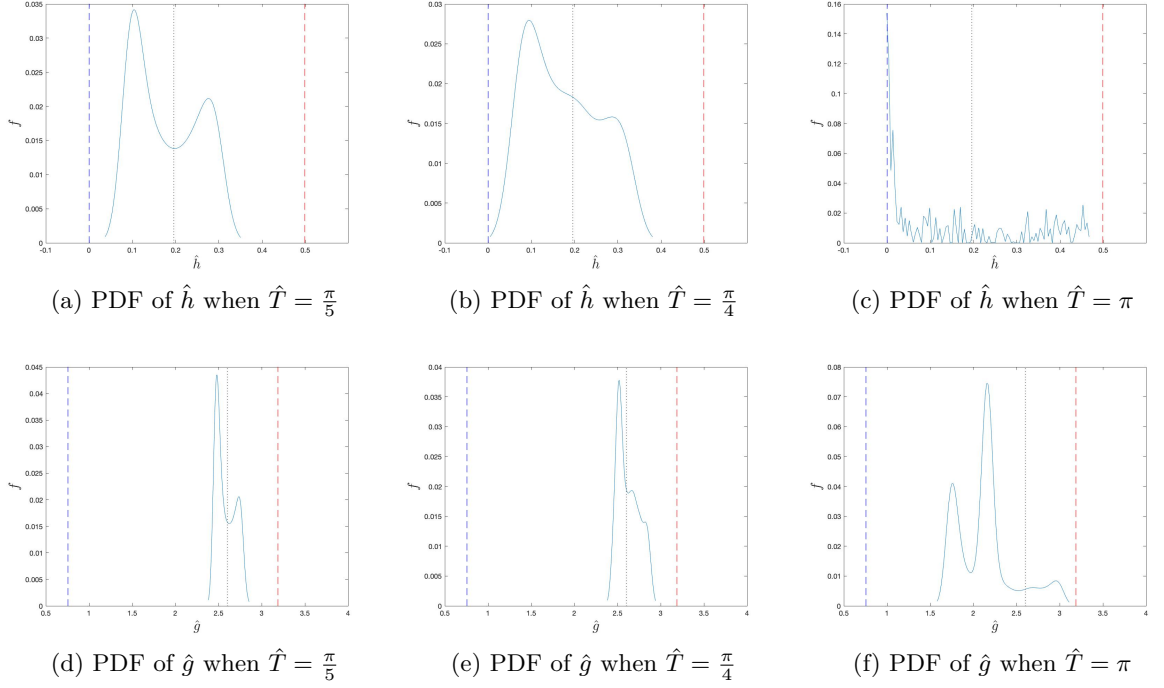
Figure 3.5: PDFs of $\hat{h}$ and $\hat{g}$ during their dynamical equilibrium when the wind parameter $W(\hat{t})$ evolves as a square wave of period $\hat{T} = \frac{\pi}{5}, \frac{\pi}{4}, \pi$ taking values 1.5 and 2.5. The venting parameter is $V = 1$. In the first row (3.5a,3.5b,3.5c) PDFs of the variable $\hat{h}$ are reported, in the second row (3.5d, 3.5e, 3.5f) are shown. In all the plots, the black dotted line is the expected value around which $\hat{h}$ or $\hat{g}$ fluctuate, obtained by system given by Equations 3.2; red dashed line refers to the steady state driven by Regime $\mathcal{A}$ when the wind parameter $W(\hat{t})$ is constant and equal to $W_0 = 2$; blue dashed line refers to the steady solution relative to Regime $\mathcal{C}$ when $W(\hat{t}) = 2$.

Figure 3.6: Time series of the wind parameter $W(\hat{t})$, their relative time series of $\hat{h}(\hat{t})$, $\hat{g}(\hat{t})$, and the distribution of $\hat{h}(\hat{t})$, $\hat{g}(\hat{t})$, when $V = 1$, $W_0 = 1.5$, $\hat{\tau}_{wv} = 0.1$ and $C_{V,wv} = 0.05, 0.1, 0.15$. Black dashed lines in the time series of $W(\hat{t})$ refer to the bifurcation point. In the time series of $\hat{h}(\hat{t})$ and $\hat{g}(\hat{t})$, red dotted lines correspond to the initial values (solutions of Eq. 1.24, namely the steady solution when Regime $\mathcal{A}$ is in force and $W(\hat{t}) = W_0$) and the red dashed lines refer to the expected values $\hat{h}_{eq}$ and $\hat{g}_{eq}$ obtained from the system given by Equations 3.2. In the PDFs of $\hat{h}$ and $\hat{g}$, the black dotted lines refer to $\hat{h}_{eq}$ and $\hat{g}_{eq}$, respectively, the red dashed lines to the solution of Eq. 1.24 (steady state when Regime $\mathcal{A}$ is in force) when $W(\hat{t}) = W_{up}$, the blue dashed lines to the steady solution of 1.25 (stable steady state when Regime $\mathcal{C}$ is in force) when $W(\hat{t}) = W_{down}$.

Figure 3.7: Time series of the wind parameter $W(\hat{t})$, their relative time series of $\hat{h}(\hat{t})$, $\hat{g}(\hat{t})$, and the distribution of $\hat{h}(\hat{t})$, $\hat{g}(\hat{t})$, when $V = 1$, $W_0 = 2$, $\hat{\tau}_{wv} = 0.1$ and $C_{V,wv} = 0.05, 0.1, 0.15$. Black dashed lines in the time series of $W(\hat{t})$ refer to the bifurcation point. In the time series of $\hat{h}(\hat{t})$ and $\hat{g}(\hat{t})$, red dotted lines correspond to the initial values (solutions of Eq. 1.24, namely the steady solution when Regime $\mathcal{A}$ is in force and $W(\hat{t}) = W_0$) and the red dashed lines refer to the expected values $\hat{h}_{eq}$ and $\hat{g}_{eq}$ obtained from the system given by Equations 3.2. In the PDFs of $\hat{h}$ and $\hat{g}$, the black dotted lines refer to $\hat{h}_{eq}$ and $\hat{g}_{eq}$, respectively, the red dashed lines to the solution of Eq. 1.24 (steady state when Regime $\mathcal{A}$ is in force) when $W(\hat{t}) = W_{up}$, the blue dashed lines to the steady solution of 1.25 (stable steady state when Regime $\mathcal{C}$ is in force) when $W(\hat{t}) = W_{down}$.
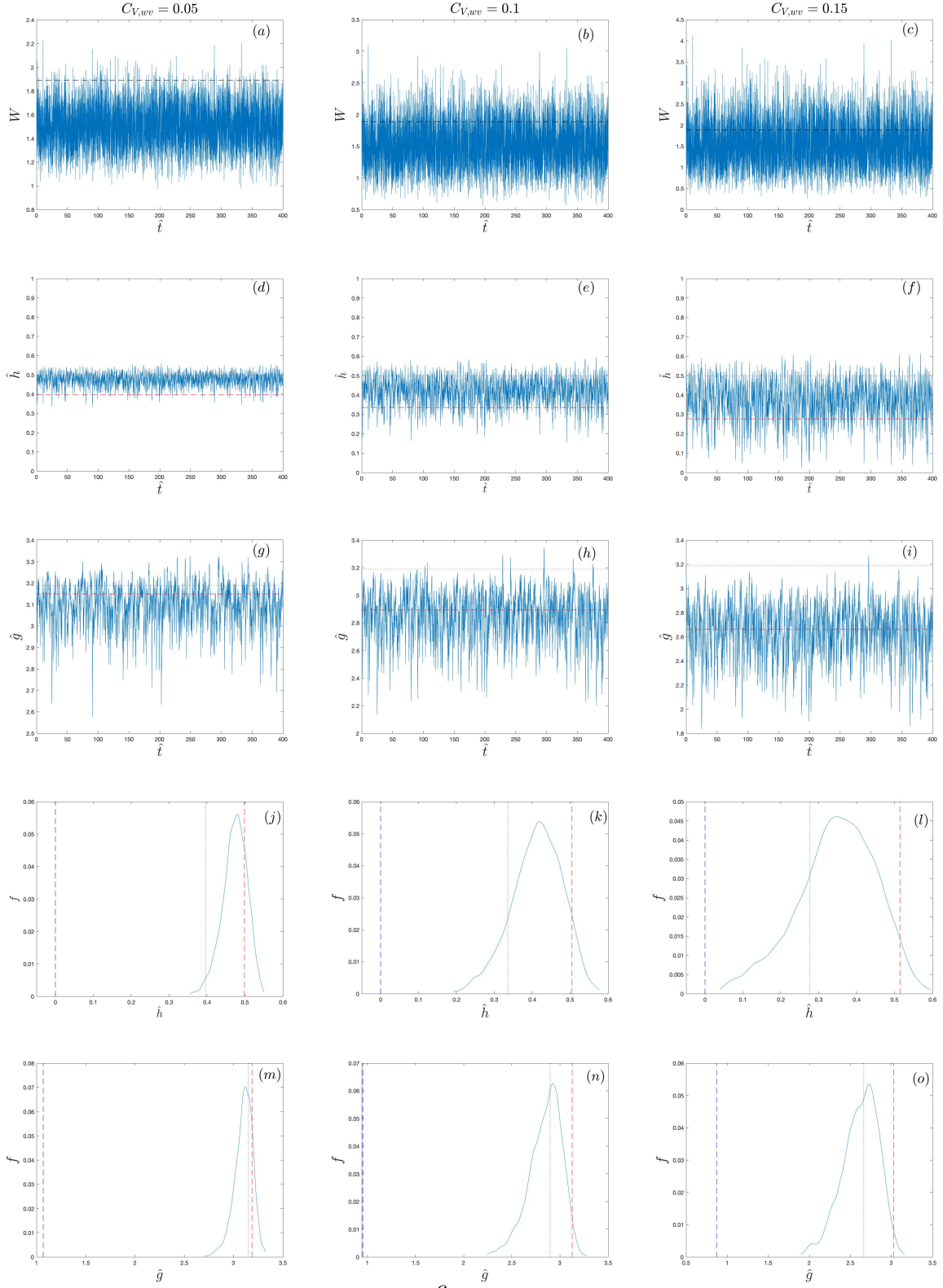
Figure 3.8: Time series of the wind parameter $W(\hat{t})$, their relative time series of $\hat{h}(\hat{t})$, $\hat{g}(\hat{t})$, and the distribution of $\hat{h}(\hat{t})$, $\hat{g}(\hat{t})$, when $V = 1$, $W_0 = 2.5$, $\hat{\tau}_{wv} = 0.1$ and $C_{V,wv} = 0.05, 0.1, 0.15$. Black dashed lines in the time series of $W(\hat{t})$ refer to the bifurcation point. In the time series of $\hat{h}(\hat{t})$ and $\hat{g}(\hat{t})$, red dotted lines correspond to the initial values (solutions of Eq. 1.24, namely the steady solution when Regime $\mathcal{A}$ is in force and $W(\hat{t}) = W_0$) and the red dashed lines refer to the expected values $\hat{h}_{eq}$ and $\hat{g}_{eq}$ obtained from the system given by Equations 3.2. In the PDFs of $\hat{h}$ and $\hat{g}$, the black dotted lines refer to $\hat{h}_{eq}$ and $\hat{g}_{eq}$, respectively, the red dashed lines to the solution of Eq. 1.24 (steady state when Regime $\mathcal{A}$ is in force) when $W(\hat{t}) = W_{up}$, the blue dashed lines to the steady solution of 1.25 (stable steady state when Regime $\mathcal{C}$ is in force) when $W(\hat{t}) = W_{down}$.
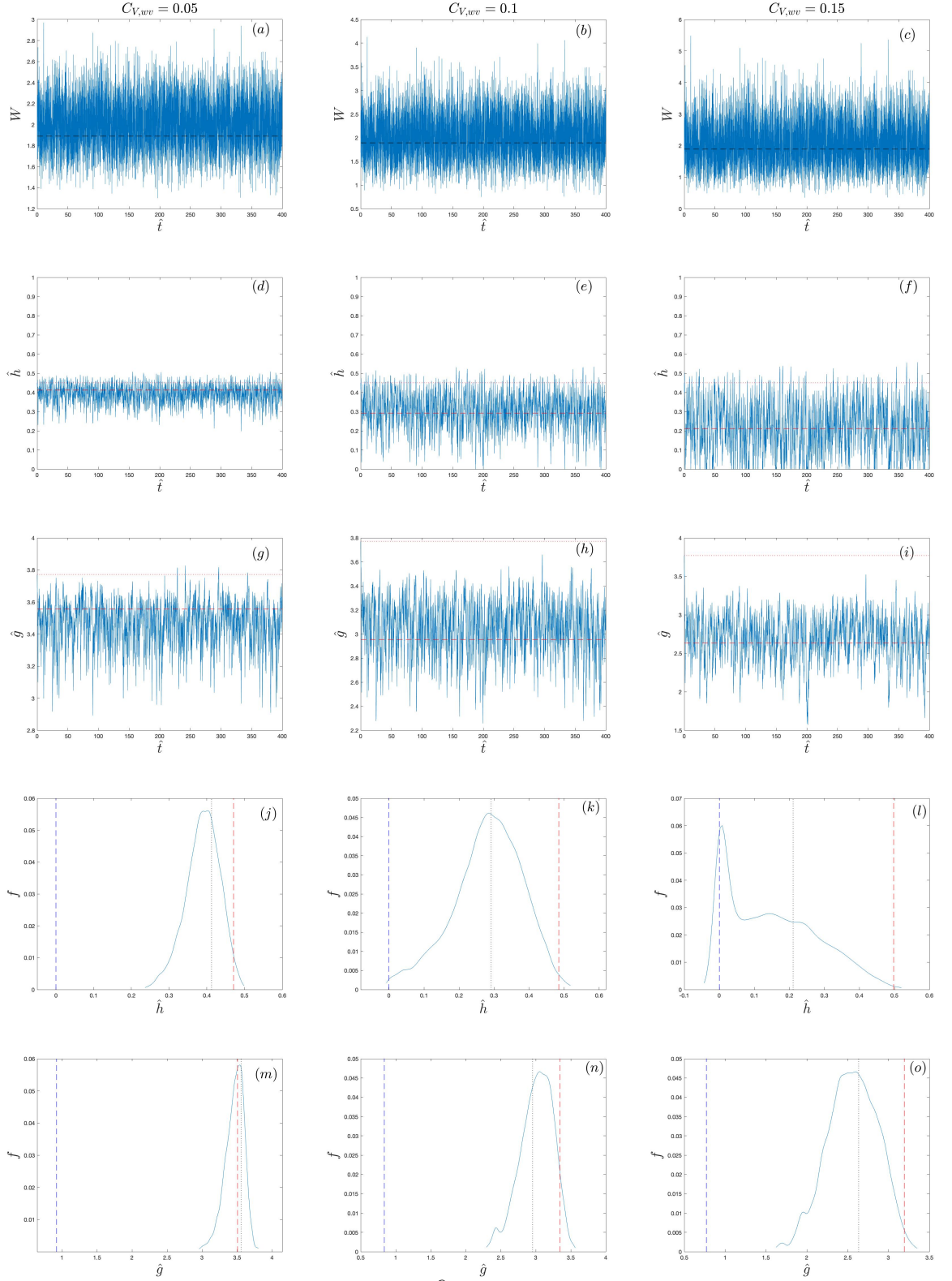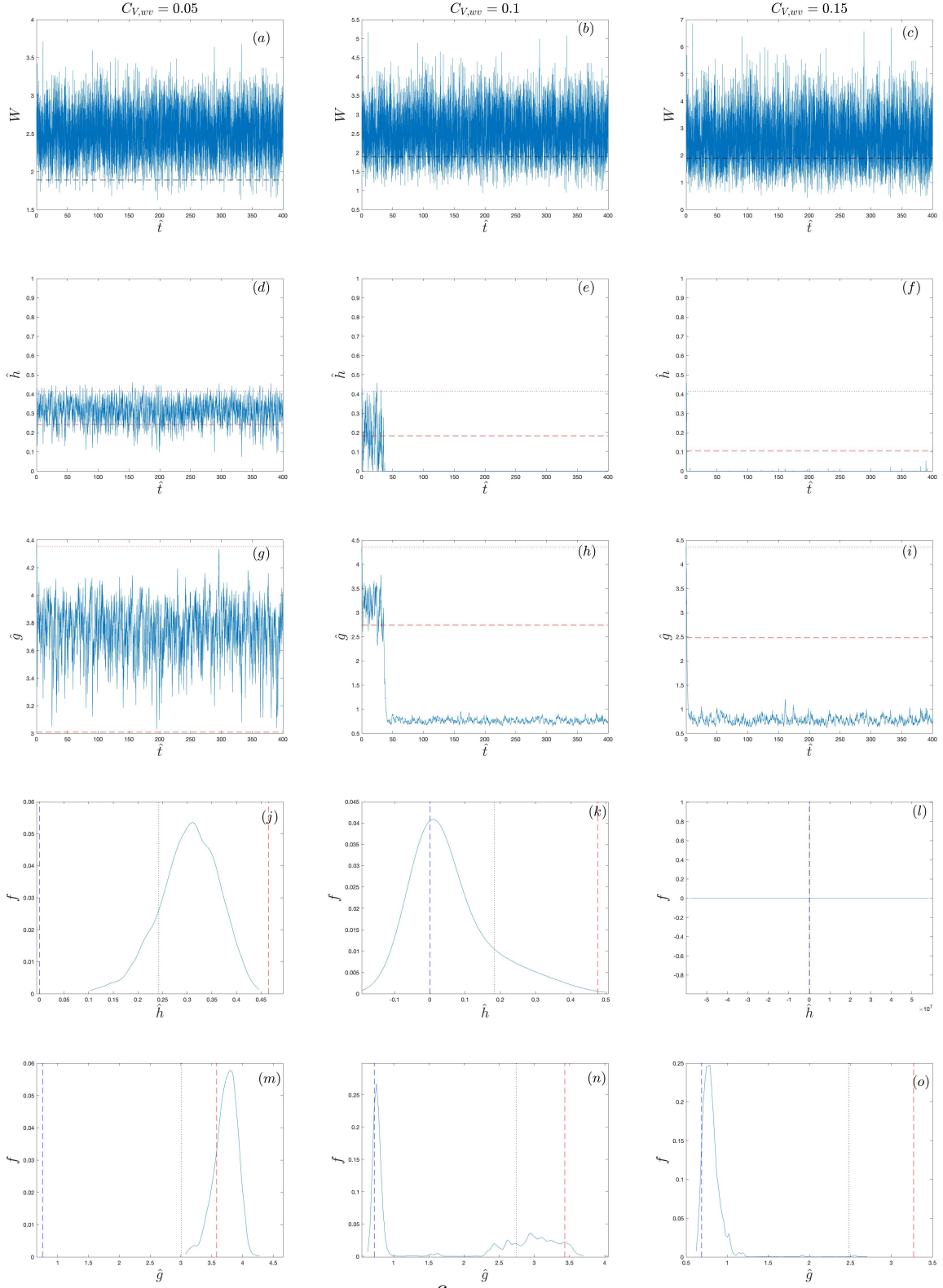
Chapter 4

Experimental campaign

In this chapter we will present the experimental campaign conducted at the Laboratoire de Mécanique des Fluides et d'Acoustique (LMFA) at the École Centrale de Lyon. Several previous works [Coomaraswamy and Caulfiled, 2011, Hunt and Linden, 2001, 2005] report experimental results concerning the case of deterministic wind-induced dynamics. Our campaign aimed to take into account the wind fluctuations, and verify if the experiments are in agreeement with the theoretical predictions.

In the following, firstly we will explain the experimental set-up that was used; secondly, we will illustrate the experiments performed and the experimental results obtained.

4.1   Experimental set-up

Experiments are performed using a transparent box which represents the room. The box is 29.5 cm long, 15 cm wide and 25 cm high, with respect to the inner of the box. Two rows of five circular holes (each of diameter 2 cm) are cut into both the windward and leeward faces at high and low levels (20 holes in total). The total opening, and thus the geometry of the system and the venting parameter V, is controlled by blocking some of these holes with rubber bungs. In all the considered configurations, all the holes on the windward face at high level and all the holes on the leeward face at low level are blocked. The effect of the wind is recreated by positioning the box in a closed-circuit wind tunnel (see Figure 4.1). The test section of this tunnel is 8 m long, 1 m high and 0.7 m wide. By controlling the mean speed of flow in the wind tunnel, we vary the mean dynamic pressure difference Δp_w between the windward and leeward sides of the box, measured directly using a manometer. This way, the mean wind parameter W is varied (recall Eq. 1.7). Wind fluctuations are obtained by placing a bluff body upwind the box: when the incoming uniform flow passes the bluff body, a vortex shedding occurs, generating alternating low-pressure vortices on the downstream side of it. This way, fluctuations of wind velocity arise. The magnitude of such fluctuations depend on the distance from the bluff body; thus, different values of the coefficient of variation of the wind velocity are attained by placing the bluff body at difference locations with respect to the box.

The buoyancy source is reproduced by the injection of carbon dioxide through a circular nozzle (diameter $0.9\ cm$) positioned in the centre of the top box. Since the carbon dioxide is heavier than the external air, in this experimental set-up the bottom of the box represents the ceiling of the room, while the top of the box represents the floor.

The carbon dioxide flux carries also a small amount of nebulized oil. This is necessary to detect the buoyancy layer and the interface, by using a laser plane. Experiments are filmed, and video processing allows the elevation of the interface between the two layers to be continuously measured. The reduced gravity in the buoyancy layer is also estimated from measures taken by a carbon dioxide sensor.
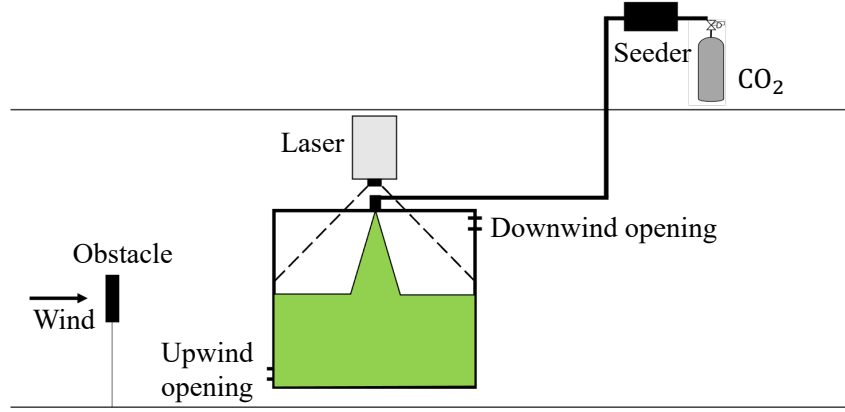
Figure 4.1: Schematic diagram of the experimental set-up, lateral view (w.r.t. the direction of the wind). The test apparatus represented is inside the closed-circuit wind tunnel. Green shaded area refers to the carbon dioxide seeded with oil, which is injected through the nozzle and visualised by means of a laser plane.

We differ from previous studies [Coomaraswamy and Caulfiled, 2011, Hunt and Linden, 2001, 2005] by using a wind tunnel instead of a flume tank: in the mentioned works the buoyancy layer is recreated by the injection of salt solution in fresh water. Despite this difference, in any case the experimental representation results upside-down with respect to the physical model: the bottom of the box stands for the ceiling of the room, while the top of the box represents the floor.

As mentioned above, we measure the interface between the two layers by processing videos taken by a camera. To do that, we need to provide a reference for the frames of the video to compute $\hat{h}$. Such a reference is supplied as described in the following.

The frame comes with a vertical resolution of $\mathcal{P} = 1080$ pixels. The frame is put in a AutoCAD box of height $\mathcal{H}$. The reference of the frame is the top-left corner (the pixel 1 is at the top of the red box, the pixel 1801 is at the bottom of the red box, see Fig. 4.2). Provided the position of the interface y'_P in pixel in the reference of the frame, this position can be converted to a position in mm in the AutoCAD reference put at the
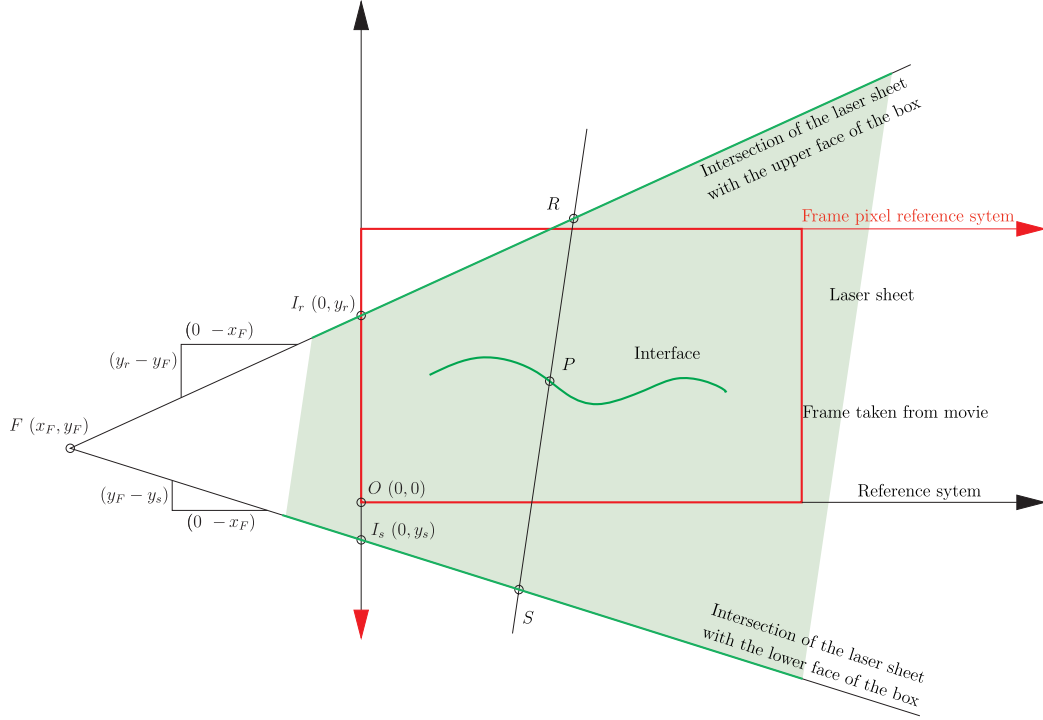
Figure 4.2: Schematic diagram of the reference of the frame (in pixel, red box and arrows) and the AutoCAD reference (in mm, black arrows) used to convert the elevation of the interface in pixel to a position in mm, later rescaled with the height of the experimental box. Green dashed area represents the lase plane.

bottom left corner of the frame (see Fig. 4.2) with the relation

$$y_P = (\mathcal{P} + 1 - y'_P)\frac{\mathcal{H}}{\mathcal{P}} = (1081 - y'_P)\frac{\mathcal{H}}{1080}. \tag{4.1}$$

The line that contains the intersection between the laser sheet and the upper face of the box has equation

$$y - y_r = x\frac{y_r - y_F}{0 - x_F}. \tag{4.2}$$

The line that contains the intersection between the laser sheet and the lower face of the box has equation

$$y - y_s = x\frac{y_s - y_F}{0 - x_F}. \tag{4.3}$$

The line that passes from P with the same inclination of all the vertical lines has equation

$$y - y_P = (x - x_P)i, \tag{4.4}$$

67

where i is the inclination of the vertical lines. Since the focus of vertical line is set very high, we suppose that all vertical lines keep parallel in the photograph and have an inclination i.

The point R is thus the intersection between the lines described by Eqs. 4.2 and 4.4. The coordinates of this point are

$$x_R = \frac{y_r + x_P i - y_P}{\frac{y_r - y_F}{x_F} + i} \tag{4.5}$$

and

$$y_R = \frac{-(y_r - y_F)}{x_F} x_R + y_r. \tag{4.6}$$

The point S is the intersection between the lines described by Eqs. 4.3 and 4.4. The coordinates of this point are

$$x_S = \frac{y_s + x_P i - y_P}{\frac{y_s - y_F}{x_F} + i} \tag{4.7}$$

and

$$y_S = \frac{-(y_s - y_F)}{x_s} x_s + y_s. \tag{4.8}$$

The total height of the room is

$$H = \sqrt{(x_R - x_S)^2 + (y_R - y_S)^2}. \tag{4.9}$$

The height of the interface is

$$h = \sqrt{(x_R - x_P)^2 + (y_R - y_P)^2}. \tag{4.10}$$

The dimensionless height of the interface is

$$\hat{h} = H/h. \tag{4.11}$$

4.2 Results

4.2.1 Characterisation of the flow field

Since we are interested in knowing the magnitude of the fluctuations of wind velocity downwind the bluff body, at the beginning we characterised the flow field inside the wind tunnel. In order to do that, firstly we measured by means of a hot wire anemometry the mean velocity $\underline{u}$ of the flow in the absence of the bluff body. This way, we associated different mean velocities at given rpms of the wind tunnel fan. As expected, we observed an uniform flow field (outside the boundary layer).

Secondly, we placed the bluff body inside the wind tunnel - at height $z \approx 475\ mm$ - and we measured at difference locations from it the mean wind velocity and its fluctuations - by means of a Pitot tube and a hot wire anemometry, respectively. In Figure 4.3 the profile of the coefficient of variation of wind velocity $C_{V,wv} = \sigma_u/\underline{u}$ is shown. On the x-axis the

distance in *mm* from the bluff body is reported, while on the *y*-axis the height *z* in *mm* from the floor of the wind tunnel is reported. Note that we display the vertical profile starting from $z = 200$ to avoid the boundary layer; we are not interested in it because the experimental box is placed at sufficient height to not be affected by the boundary layer. As expected, the profile reported in Fig. 4.3 is obtained for any mean velocity $\underline{u}$: changing rpm of the wind tunnel fan does not effect the behaviour of the magnitude of the fluctuations $\sigma_u/\underline{u}$.
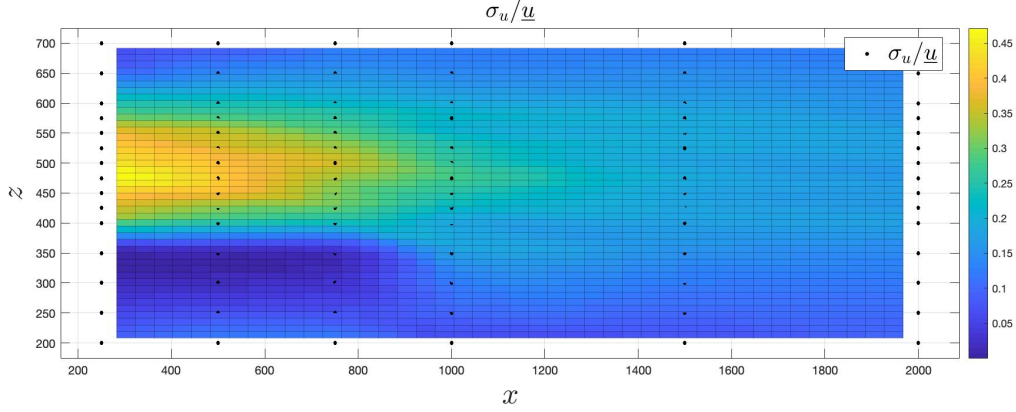
Figure 4.3: Vertical profile of the coefficient of variation of wind velocity $C_{V,wv} = \sigma_u/\underline{u}$. Both the distance reported on the *x*-axis - distance from the bluff body - and on the *y*-axis - height *z* from the floor of the wind tunnel - are in *mm*.

4.2.2   Preliminary investigation

In order to validate our experimental campaign and to confirm that in absence of wind the system behaves as we expect, firstly we verified that in steady-state condition when no wind occurs the elevation of the interface $\hat{h}$ does not depend on the buoyancy flux B (recall the description of the problem in Section 1.1.1).

To do that, we considered different geometries of the system, namely different venting parameter V, by changing the number and the order of the open holes on the windward and leeward faces. To keep the same discharge coefficient for both the openings - i.e. to keep c_B and c_T in Eq. 1.1 equal - we maintained the same configuration of holes blocked or unblocked on the windward and leeward faces. By referring to unblocked holes as 'O' and to blocked holes as 'X', we mention the considered configurations as: 'OXXXO', 'XOXOX', 'OXOXO', 'XOOOX', 'OOXOO', 'OOOOO', 'XXOXX'. Note that all the geometries taken into account are symmetric.

For each configuration, we measured the height of the interface $\hat{h}$ changing the source buoyancy flux. It is convenient to write the buoyancy flux in terms of a dimentionless number which expresses the ratio between the buoyancy and the flow terms at the physical source [Morton, 1959, Michaux and Vauquelin, 2008, Morton and Middleton, 1973, Hunt

69

and Kaye, 2001], namely a Richardson number

$$\Gamma = \frac{5}{8\alpha\sqrt{\pi}} g' \frac{r}{w^2}, \qquad (4.12)$$

where r is the radius of the nozzle in the experimental set-up while w is the vertical velocity of the plume at the source and reads

$$w = \frac{Q}{A}, \qquad (4.13)$$

with A area of the nozzle and Q flow rate of the carbon dioxide injected through the nozzle.

In Figure 4.4 we report the behaviour of the level of the interface $\hat{h}$ for the considered configurations, for different Richardson number Γ, and thus different source buoyancy flux. As expected, the height of the interface between the warm and cold layers is not effected by the buoyancy at the source when no wind occurs. Note that considering $\Gamma > 1$
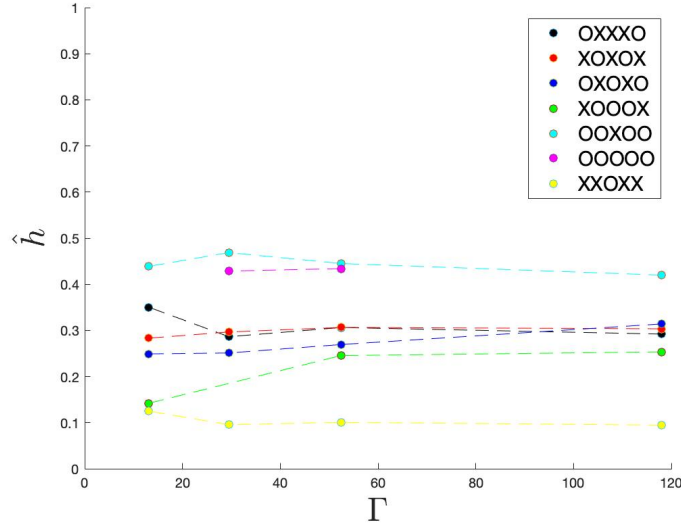
Figure 4.4: Elevation of the interface $\hat{h}$ in steady-state conditions when no wind occurs for different source buoyancy fluxes, and thus different Richardson numbers Γ.

we are taking into account lazy plumes, i.e. plumes dominated by buoyancy instead of momentum [Mehaddi et al., 2021, Morton, 1959].

4.2.3 Further investigation

The main investigation conducted aimed to consider wind fluctuations and verify if the experimental results are in agreement with the theoretical predictions illustrated in Chapter 2. To do that, we were interested in observing the response of the system when forced

by wind fluctuations, and how the response changes when the system undergoes different forcing with different magnitude of fluctuations. For this reason, our intent was to investigate the behaviour of the reduced gravity $\hat{g}$ and the elevation of the interface $\hat{h}$ for different wind velocities and wind fluctuations, keeping fixed the geometry of the system and the flow and buoyancy terms at the physical source. Recalling the notation mentioned in the previous Section (4.2.2), the configuration chosen for our study was 'OXXXO', as done in previous literature [Coomaraswamy and Caulfiled, 2011]. The Richardson number considered for the experimental campaigned was $\Gamma \approx 20$.

In Figure 4.5 the experimental results (markers) and the expected behaviour from theory in case of constant wind (black lines) are reported. Firstly, we notice that there

(a) Experimental results for $\hat{g}$. (b) Experimental results for $\hat{h}$.
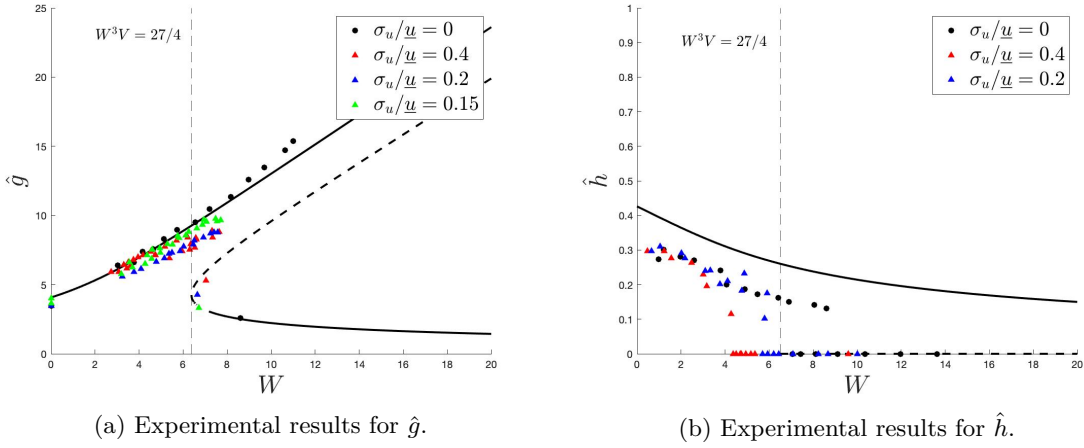
Figure 4.5: Experimental results (markers) obtained for different magnitude of wind fluctuations, and theoretical prediction in case of constant wind (black lines). Thin dashed vertical line indicates the bifurcation condition predicted by the theoretical model.

is a variance between the theoretical prediction and experimental results regarding the elevation of the interface $\hat{h}$ (see Fig. 4.5b): such a difference is attributable to the fact that the mathematical model considers a point buoyancy source, whereas in the experimental set-up the buoyancy source has a non-zero diameter. Therefore, we should take into account a point virtual origin [Mehaddi et al., 2021, Michaux and Vauquelin, 2008] placed under the physical origin, thanks to which the theoretical buoyancy source described by the model is satisfied. Adding the height of such virtual origin to the interface elevation $\hat{h}$ measured from experiments we expect to smooth the difference between the mathematical model and the experimental results.

Secondly, regardless the variance mentioned above, we see that in case of constant wind (black circle), the results are in agreement with the theoretical prediction and fit the theoretical curve very well. When wind fluctuations occur (coloured triangles), we remark three different behaviours.

- For low values of W, the effect of wind fluctuations is almost negligible and black

and coloured markers are comparable.

- As W approaches the bifurcation point, effects of wind fluctuations become more and more severe: both the reduced gravity $\hat{g}$ and the interface height $\hat{h}$ are much lower than the ones obtained in case of constant wind (compare black circles and coloured triangles: all the coloured markers - $\sigma_u/\underline{u} > 0$ - are below the black circles). Such a difference increases as W increases.

- The transition to Regime $\mathcal{C}$ occurs for lower values of W when $\sigma_u/\underline{u} > 0$. This can be deduced because the lowest value of W at which transition to Regime $\mathcal{C}$ takes place is associated with the highest value of $\sigma_u/\underline{u} > 0$.

All these behaviours are expected from the theoretical study (recall Chapter 2).

Conclusions

This work aimed to investigate the dynamics of a naturally ventilated system, namely a room characterised by the presence of a point buoyancy source submitted to the action of an external opposing wind. Differently from previous works on ventilated systems, we considered an unsteady wind, modelled by adding a stochastic forcing to the government equations. We are interested in the effect of wind fluctuations on two variables of the system: the height of the interface between the layer of cool ambient air and the buoyant layer, that accumulates on the ceiling of the room, and its reduced gravity. Our study highlights that the time-average elevation attained in presence of fluctuating wind can be much different (lower) from the height observed in case of constant wind. The interface elevation tends to decrease, and so does the reduced gravity of the buoyant layer.

We investigated this counterintuitive behaviour, firstly following a theoretical approach. Indeed, in the first place we analysed how this observed difference is affected by (i) the intensity and relaxation time of wind fluctuations, (ii) the vent and wind parameters. From this parametric study, we found out that most of these parameters have a relevant effect on the dynamics of the system; the only parameter whose effect is marginal is the relaxation time of wind fluctuations. Furthermore, we provided a physical explanation of the phenomenon.

Secondly, we performed an experimental campaign in order to validate the theoretical results. The results obtained are in agreement with the outcomes of the theoretical study. When a stochastic forcing occurs, an alteration of the time-averaged dynamics of the ventilated system is observed. Moreover, the effect of both the wind parameter and the intensity of wind fluctuations is proved. Indeed, as the magnitude of the coefficient of variation of wind velocity increases, the alteration observed increases. Furthermore, transition to fully mixed regime takes place for lower values of the wind parameter.

This study requires further developments: it is planned to process all the collected data not treated yet and to obtain more robust statistics on them.

In the end, it should be noticed that the scientific community is increasingly highlighting the role of stochastic components in inducing structural changes in the behaviour of a dynamic systems - the so-called "noise-induced phenomena". This work shows as also natural ventilation exhibits this fascinating feature, which should be considered for effective design, given the ubiquity of wind fluctuations.

Bibliography

J. Pablo Arenas-López and Mohamed Badaoui. Stochastic modelling of wind speeds based on turbulence intensity. *Renewable Energy*, 155:10–22, 2020. ISSN 0960-1481. doi: https://doi.org/10.1016/j.renene.2020.03.104. URL https://www.sciencedirect.com/science/article/pii/S0960148120304365.

W. D. Baines and J. S. Turner. Turbulent buoyant convection from a source in a confined region. *Journal of Fluid Mechanics*, 37(1):51–80, 1969. doi: 10.1017/S0022112069000413.

G.K. Batchelor, H.K. Moffatt, and M.G. Worster. *Perspectives in Fluid Dynamics: A Collective Introduction to Current Research*. Cambridge University Press, 2003. ISBN 9780521531696.

Rajesh K. Bhagat, M. S. Davies Wykes, Stuart B. Dalziel, and P. F. Linden. Effects of ventilation on the indoor spread of covid-19. *Journal of Fluid Mechanics*, 903:F1, 2020. doi: 10.1017/jfm.2020.720.

Diogo Bolster. Transients in natural ventilation — a time-periodically-varying source. *Building Services Engineering Research and Technology - BUILD SERV ENG RES TECHNOL*, 29:119–135, 05 2008. doi: 10.1177/0143624407087849.

D. J. Bower, C. P. Caulfield, S. D. Fitzgerald, and A. W. Woods. Transient ventilation dynamics following a change in strength of a point source of heat. *Journal of Fluid Mechanics*, 614:15–37, 2008. doi: 10.1017/S0022112008003479.

I. A. Coomaraswamy and C. P. Caulfiled. Time-dependent ventilation flows driven by opposing wind and buoyancy. *Journal of Fluid Mechanics*, 672:33–59, 2011.

John Craske and Graham O. Hughes. On the robustness of emptying filling boxes to sudden changes in the wind. *Journal of Fluid Mechanics*, 868:R3, 2019. doi: 10.1017/jfm.2019.199.

Eric Doorn, Brindesh Dhruva, Katepalli Sreenivasan, and Victor Cassella. Statistics of wind direction and its increments. *Physics of Fluids*, 12, 06 2000. doi: 10.1063/1.870401.

M. Economidou and G.R. Hunt. Transient flows in enclosures: A generalised approach for modelling the effects of geometry, heat gains and wind. *Building and Environment*, 45(12):2607–2619, 2010. ISSN 0360-1323. doi: https://doi.org/10.1016/

j.buildenv.2010.05.020. URL https://www.sciencedirect.com/science/article/pii/S0360132310001587.

Paul Edwards and Robert Hurst. Level-crossing statistics of the horizontal wind speed in the planetary surface boundary layer. *Chaos (Woodbury, N.Y.)*, 11:611–618, 10 2001. doi: 10.1063/1.1379310.

Anthony Fontanini, Umesh Vaidya, and Baskar Ganapathysubramanian. A stochastic approach to modeling the dynamics of natural ventilation systems. *Energy and Buildings*, 63:87–97, 2013. ISSN 0378-7788. doi: https://doi.org/10.1016/j.enbuild.2013.03.053. URL https://www.sciencedirect.com/science/article/pii/S0378778813002223.

Daniel T. Gillespie. Exact numerical simulation of the ornstein-uhlenbeck process and its integral. *Phys. Rev. E*, 54:2084–2091, Aug 1996. doi: 10.1103/PhysRevE.54.2084.

Anhui Gu, Boling Guo, and Bixiang Wang. Long term behavior of random navier-stokes equations driven by colored noise, 2020. ISSN 1531-3492.

Per Heiselberg, Yuguo Li, A Andersen, M Bjerre, and Z Chen. Experimental and cfd evidence of multiple solutions in a naturally ventilated building. *Indoor air*, 14:43–54, 03 2004. doi: 10.1046/j.1600-0668.2003.00209.x.

Joanne M. Holford and Gary R. Hunt. Fundamental atrium design for natural ventilation. *Building and Environment*, 38(3):409–426, 2003. ISSN 0360-1323. doi: https://doi.org/10.1016/S0360-1323(02)00019-7. URL https://www.sciencedirect.com/science/article/pii/S0360132302000197.

G. Hunt and Andrew Acred. Passive ventilation in multi-storey atrium buildings: A first-order design guide. 09 2013.

G. R. Hunt and N. G. Kaye. Virtual origin correction for lazy turbulent plumes. *Journal of Fluid Mechanics*, 435:377–396, 2001. doi: 10.1017/S0022112001003871.

G. R. Hunt and P. F. Linden. Steady-state flows in an enclosure ventilated by buoyancy forces assisted by wind. *Journal of Fluid Mechanics*, 426:355–386, 2001. doi: 10.1017/S0022112000002470.

G. R. Hunt and P. F. Linden. Displacement and mixing ventilation driven by opposing wind and buoyancy. *Journal of Fluid Mechanics*, 527:27–55, 2005.

G.R. Hunt and P.P. Linden. The fluid mechanics of natural ventilation—displacement ventilation by buoyancy-driven flows assisted by wind. *Building and Environment*, 34 (6):707–720, 1999. ISSN 0360-1323.

N. B. Kaye and G. R. Hunt. Time-dependent flows in an emptying filling box. *Journal of Fluid Mechanics*, 520:135–156, 2004. doi: 10.1017/S0022112004001156.

Andrea S. Kuesters and Andrew W. Woods. The formation and evolution of stratification during transient mixing ventilation. *Journal of Fluid Mechanics*, 670:66–84, 2011. doi: 10.1017/S0022112010005392.

G. F. Lane-Serff and S. D. Sandbach. Emptying non-adiabatic filling boxes: the effects of heat transfers on the fluid dynamics of natural ventilation. *Journal of Fluid Mechanics*, 701:386–406, 2012. doi: 10.1017/jfm.2012.164.

P. F. Linden. The fluid mechanics of natural ventilation. *Annual Review of Fluid Mechanics*, 31(1):201–238, 1999. doi: 10.1146/annurev.fluid.31.1.201.

P. F. Linden, G. F. Lane-Serff, and D. A. Smeed. Emptying filling boxes: the fluid mechanics of natural ventilation. *Journal of Fluid Mechanics*, 212:309–335, 1990. doi: 10.1017/S0022112090001987.

B. Lishman and A. W. Woods. The control of naturally ventilated buildings subject to wind and buoyancy. *Journal of Fluid Mechanics*, 557:451–471, 2006. doi: 10.1017/S0022112006009931.

Ben Lishman and Andrew W. Woods. On transitions in natural ventilation flow driven by changes in the wind. *Building and Environment*, 44(4):666–673, 2009a. ISSN 0360-1323. doi: https://doi.org/10.1016/j.buildenv.2008.05.012. URL https://www.sciencedirect.com/science/article/pii/S0360132308001091.

Ben Lishman and Andrew W. Woods. The effect of gradual changes in wind speed or heat load on natural ventilation in a thermally massive building. *Building and Environment*, 44(4):762–772, 2009b. ISSN 0360-1323. doi: https://doi.org/10.1016/j.buildenv.2008.06.026. URL https://www.sciencedirect.com/science/article/pii/S0360132308001340.

Jinrui Ma, Mitra Fouladirad, and Antoine Grall. Flexible wind speed generation model: Markov chain with an embedded diffusion process. *Energy*, 164:316–328, 2018. ISSN 0360-5442. doi: https://doi.org/10.1016/j.energy.2018.08.212.

R. Mehaddi, P. Boulet, M. Koutaiba, O. Vauquelin, and F. Candelier. Emptying-filling boxes with non-boussinesq plumes and fountains. *Phys. Rev. Fluids*, 6:083801, Aug 2021. doi: 10.1103/PhysRevFluids.6.083801. URL https://link.aps.org/doi/10.1103/PhysRevFluids.6.083801.

Ghislain Michaux and Olivier Vauquelin. Solutions for turbulent buoyant plumes rising from circular sources. *Physics of Fluids - PHYS FLUIDS*, 20, 06 2008. doi: 10.1063/1.2926758.

H. Montazeri and B. Blocken. Cfd simulation of wind-induced pressure coefficients on buildings with and without balconies: Validation and sensitivity analysis. *Building and Environment*, 60:137–149, 2013. ISSN 0360-1323. doi: https://doi.org/10.1016/j.buildenv.2012.11.012. URL https://www.sciencedirect.com/science/article/pii/S0360132312003101.

Miguel Mora-Pérez, Ignacio Guillén-Guillamón, and P. Amparo López-Jiménez. Computational analysis of wind interactions for comparing different buildings sites in terms of natural ventilation. *Advances in Engineering Software*, 88:73–82, 2015.

ISSN 0965-9978. doi: https://doi.org/10.1016/j.advengsoft.2015.06.003. URL https://www.sciencedirect.com/science/article/pii/S0965997815000897.

B. R. Morton. Forced plumes. *Journal of Fluid Mechanics*, 5(1):151–163, 1959. doi: 10.1017/S002211205900012X.

B. R. Morton and Jason Middleton. Scale diagrams for forced plumes. *Journal of Fluid Mechanics*, 58(1):165–176, 1973. doi: 10.1017/S002211207300220X.

Bruce R. Morton, Geoffrey Ingram Sir Taylor, and John Stewart Turner. Turbulent gravitational convection from maintained and instantaneous sources. *Proceedings of the Royal Society of London. Series A. Mathematical and Physical Sciences*, 234:1 – 23, 1956.

Richard W. Mott and Andrew W. Woods. Natural ventilation driven by periodic gusting of wind. *Journal of Fluid Mechanics*, 679:58–76, 2011. doi: 10.1017/jfm.2011.122.

Richard W. Mott and Andrew W. Woods. Quasi-steady states in natural displacement ventilation driven by periodic gusting of wind. *Journal of Fluid Mechanics*, 707:1–23, 2012. doi: 10.1017/jfm.2012.230.

Luca Ridolfi, Paolo D'Odorico, and Francesco Laio. *Index*, page 311–313. Cambridge University Press, 2011.

Anastasia D. Stavridou and Panagiotis E. Prinos. Natural ventilation of buildings due to buoyancy assisted by wind: Investigating cross ventilation with computational and laboratory simulation. *Building and Environment*, 66:104–119, 2013. ISSN 0360-1323. doi: https://doi.org/10.1016/j.buildenv.2013.04.011. URL https://www.sciencedirect.com/science/article/pii/S0360132313001169.

George. E. Uhlenbeck and Leonard S. Ornstein. On the theory of the brownian motion. *Physical Review*, 36(5):823–841, September 1930.

R. Vesipa, L. Ridolfi, and P. Salizzoni. Wind fluctuations affect the mean behaviour of naturally ventilated systems. *Building and Environment*, 229:109928, 2023.

Riccardo Vesipa, Carlo Camporeale, and L Ridolfi. Geophysical research letters noise-driven cooperative dynamics between vegetation and topography in riparian zones. *Geophysical Research Letters*, 42, 10 2015. doi: 10.1002/2015GL065688.

Riccardo Vesipa, Carlo Camporeale, and L. Ridolfi. Recovery times of riparian vegetation. *Water Resources Research*, pages n/a–n/a, 03 2016. doi: 10.1002/2015WR018490.

Riccardo Vesipa, Eleonora Paissoni, Costantino Manes, and Luca Ridolfi. Dynamics of bubbles under stochastic pressure forcing. *Physical Review E*, 103, 02 2021. doi: 10.1103/PhysRevE.103.023108.

Andrew W. Woods, C. P. Caulfield, and Jeremy C. Phillips. Blocked natural ventilation: the effect of a source mass flux. *Journal of Fluid Mechanics*, 495:119–133, 2003. doi: 10.1017/S0022112003005627.

M. Grae Worster and Herbert E. Huppert. Time-dependent density profiles in a filling box. *Journal of Fluid Mechanics*, 132:457–466, 1983. doi: 10.1017/S002211208300172X.

X. Yang, G. Wang, K. Zhong, and Y. Kang. Transient pollutant flushing of buoyancy-driven natural ventilation. *Building Simulation*, 5(2):147–155, 2012. doi: 10.1007/s12273-012-0077-4.

Jinchao Yuan and Leon R. Glicksman. Transitions between the multiple steady states in a natural ventilation system with combined buoyancy and wind driven flows. *Building and Environment*, 42(10):3500–3516, 2007. ISSN 0360-1323. doi: https://doi.org/10.1016/j.buildenv.2006.10.045. URL https://www.sciencedirect.com/science/article/pii/S0360132306003805.

Jinchao Yuan and Leon R. Glicksman. Multiple steady states in combined buoyancy and wind driven natural ventilation: The conditions for multiple solutions and the critical point for initial conditions. *Building and Environment*, 43(1):62–69, 2008. ISSN 0360-1323. doi: https://doi.org/10.1016/j.buildenv.2006.11.035. URL https://www.sciencedirect.com/science/article/pii/S036013230600446X.